



The where, when, and how of ooid formation: What ooids tell us about ancient seawater chemistry

Bolton Howes ^{a,*}, Akshay Mehra ^{a,b}, Emily Geyman ^{a,c}, Julia Wilcots ^a, Ryan Manzuk ^a, Curtis Deutsch ^a, Adam Maloof ^a

^a Department of Geosciences, Princeton University, Guyot Hall, Princeton, 08544, NJ, USA

^b Department of Earth and Space Sciences, University of Washington, 4000 15th Ave NE, Seattle, 98195, WA, USA

^c Division of Geological and Planetary Sciences, California Institute of Technology, Arms Laboratory, Pasadena, 91125, CA, USA

ARTICLE INFO

Editor: H. Bao

Dataset link: <https://data.mendeley.com/datasets/3zpj3bd5w4/1>

Keywords:

ooids
carbonate sediment
alkalinity
seawater chemistry

ABSTRACT

Ooids are a common constituent of carbonate rock throughout the last 3.2 billion years. The chemical and physical characteristics of ooids record essential details of the carbonate chemistry and hydrodynamic conditions of their depositional environment. As a result, ooids may be a powerful tool for reconstructing Earth's ancient climates and environments. However, lack of constraints on fundamental aspects of ooid formation, such as the role of abrasion, underscores the potential for additional discoveries utilizing ooids as paleoenvironmental proxies. Here, we use three-dimensional models built by serially grinding and imaging ooids to show how ooid shape changes during growth. We find that ooid abrasion plays only a small role in the formation of ooids, even in giant ooids, where the mass should cause abrasion to be most intense. A lack of abrasion during ooid formation suggests a greater sensitivity of ooid distribution and size to the chemistry of depositional environments. This insight enables us to harmonize our understanding of ooid formation with longstanding questions regarding their spatial and temporal distribution, as well as size variations. With a new database of ooid occurrences, we analyze the influence of seawater chemistry, carbonate shelf area, and evolutionary developments on ooid abundance in the Modern, Last Glacial Period, and throughout the Phanerozoic. Finally, we leverage our new understanding of ooid growth to show how ooid size, including giant ooids, can shed light on relative changes in alkalinity throughout the Phanerozoic.

1. Introduction

Carbonate sedimentation is both an important feedback in, and an active recorder of, seawater chemistry. Since seawater chemistry is intertwined with the carbon cycle, and by extension Earth's climate, carbonate rock provides a vital archive of our planet's climate history. Research on the carbonate chemistry of ancient oceans typically relies on geochemical measurements of rocks, often serving as proxies for parameters like alkalinity, water temperature, and the abundance of carbon dioxide (e.g. Zeebe (2012)). However, paleoenvironmental and paleoclimate interpretations derived from these measurements are complicated by the fact that carbonate geochemistry is influenced by factors other than global average seawater. For example, diagenetic processes can modify or even obliterate original geochemical signals (Higgins et al., 2018), and geochemistry can vary significantly even between adjacent facies (Geyman and Maloof, 2021), further complicating the

interpretation of these records. Fortunately, the physical characteristics of carbonate rocks also serve as recorders of *in situ* chemical parameters, which can corroborate and inform the analysis of geochemical measurements. For example, quantitative measures of shell type and abundance, original mineralogy of grains and cements, and the degree of recrystallization all can be assessed using petrographic analyses (vS Hood et al., 2018; Manzuk et al., 2022).

Here we focus on one type of physical record of seawater chemistry—ooids. Ooids are concentrically-laminated, sedimentary grains produced through successive stages of carbonate precipitation and abrasion that typically form above wave base in tropical-to-subtropical carbonate platforms (e.g., Davies et al. (1978)). Given their abundance in carbonate rocks over the last 3.2 billion years (Fig. 1) and the direct correlation between their physical and chemical makeup and the environmental conditions, ooids serve as a crucial tool for understanding the history of seawater (e.g., Wilkinson and Given (1986); Trower (2020)),

* Corresponding author.

E-mail address: bhowes@princeton.edu (B. Howes).

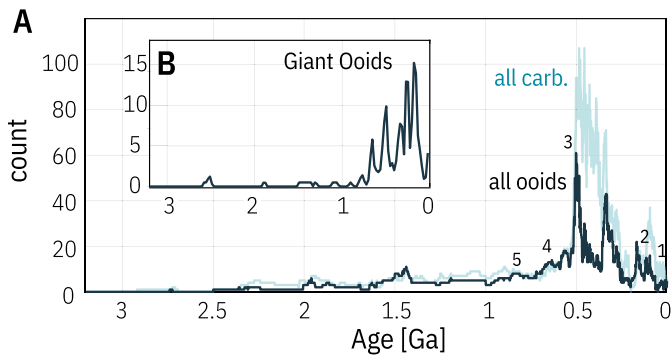


Fig. 1. The abundances of carbonates, ooids, and giant ooids in the geological record. A) Ooid and carbonate occurrences peaked in the early Paleozoic. The low quantities of ooids and carbonate rocks older than 1 Ga may reflect the low survivorship of rocks over 1 Ga (Keller et al., 2019). Data are depicted in one-million-year time bins. The samples examined in this study: (1) Great Salt Lake, (2) Great Bank of Guizhou, (3) Gatesburg Formation, (4) Etina Formation, (5) Matheos Formation. (B) Ooids with a diameter > 1 mm plotted in 20 million year time bins.

and consequently, Earth's climate. However, the prevailing model for ooid growth is in conflict with existing data about ooids and carbonate environments. This paper begins by identifying and examining the incongruencies between existing data and the prevailing model of ooid growth. We then outline our methodology, crafted to provide a more direct demonstration of the episodic nature of ooid growth. Finally, we delve into the broader implications of our results, clarifying longstanding questions about ooid abundance, distribution, and size.

1.1. The geometry of ooid growth and abrasion

Carbonate precipitation onto the ooid cortex causes an ooid to grow in a surface normal direction (Meakin and Jamtveit, 2010; Sipos et al., 2018). There is debate about the relative importance of microbial processes in mediating ooid growth, but the gross geometric outcomes of carbonate precipitation (surface-normal growth) are independent of microbial mediation (Batchelor et al., 2018; Sipos et al., 2018). Abrasion also has been hypothesized to play a role in ooid formation, with abrasion from saltation causing ooids to become more spherical, and abrasion from rolling causes ooids to become more ellipsoidal (Sipos et al., 2018). The concentric laminations of an ooid record the shape of the grain as it grows. While there are some studies of gross ooid morphology (e.g., Heller et al. (1980); Trower et al. (2018)), there are only a few studies of the morphology of ooid laminations (Heller et al., 1980; Sipos et al., 2018; Trower et al., 2020).

Studying ooid-forming environments by measuring the morphology of growth laminations presents unique challenges: (1) ooids are ellipsoidal-spherical, which can lead to errors if size and shape are measured with conventional two-dimensional methods (Howes et al., 2021), and (2) ooids abrade, which can remove portions of (or entire) laminations. But these challenges also provide insights. We make three-dimensional (3D) reconstructions to overcome the challenge presented by ooid shapes. While abrasion means that some of the record is lost, the morphological outcomes of abrasion provide a forensic opportunity to understand ooid formation. In this paper, we present 3D models of ooid growth laminae showing that abrasion plays only a minor role in ooid evolution, and that ooids are a more sensitive recorder of seawater chemistry than previously appreciated. This result affords us the ability to interpret changes in ooid distribution over time and space, as well as variations in ooid size.

1.2. Revisiting constraints on ooid growth rates

Recent efforts to infer ancient ocean conditions from ooid morphology represent a valuable addition to our geochemical toolbox for

understanding Earth's history. These efforts have hinged on specific estimates of ooid growth based on interpretations of radiocarbon ^{14}C dates from sequential leaching of ooids (Beaupré et al., 2015; Trower et al., 2017). These ^{14}C ages suggest that the lifespan of an ooid (i.e., time between nucleation and the formation of the outermost cortex) is much longer than it would take to precipitate that volume of CaCO_3 based on extrapolating any of a variety of estimates of short-term precipitation rates from lab experiments of ooid growth (Ferguson et al., 1978), empirical carbonate precipitation rate equations (Zhong and Mucci, 1989), and field measurements (Broecker and Takahashi, 1966). The ^{14}C data reveal that the outermost laminae are 80–280 years old, meaning it is possible that newly precipitated CaCO_3 is entirely removed by abrasion. Using these observations, authors have argued that much of the CaCO_3 that precipitates onto an ooid must be removed through abrasion (Trower et al., 2017). In other words, if ooids were to grow at the measured short-term CaCO_3 precipitation rates for their entire lifespans, they would be huge (10's of mm). So, the argument goes, frequent abrasion must keep ooids smaller (Trower et al., 2017).

Rapid precipitation and abrasion of CaCO_3 in this model of ooid growth contains two implicit predictions: (1) ooid shape should be heavily influenced by abrasion, and (2) the product of abrasion (mud) should bear the geochemical signature of ooids. Neither prediction is supported by previously published observations from modern environments. Modern ooids primarily are transported via saltation (Trower et al., 2020), so if ooids were rapidly precipitating and abrading for their entire lifespan, they should be highly spherical (Sipos et al., 2018). However, measurements reveal that modern ooids are consistently ellipsoidal—sub-spherical, suggesting that either abrasion during transport has not been the dominant control on their shape, or that the ooids have not reached their equilibrium shape (Fig. 2A). The persistence of irregular shapes in ooids strongly suggests that abrasion occurs at rates lower than previously thought. Furthermore, if ooids abrade enough to make up the difference between net growth rate and precipitation rates, the abrasion product would make up a substantial proportion of mud in The Bahamas (Trower et al., 2019). However, there is no geochemical evidence for ooids significantly contributing to mud in The Bahamas (Fig. 2B) (Geyman et al., 2022).

The contradiction between the high-abrasion interpretation of ^{14}C ages and the morphological and geochemical evidence led us to imagine this study, and to propose an alternative to the high-abrasion interpretation of ^{14}C ages: episodic growth. We believe that ooids have not grown at the experimental precipitation rates for the entirety of the last 800–1000 years because they have only grown during brief, infrequent episodes of transport. This interpretation of the ^{14}C ages of ooids is in line with classical models of ooid growth that include brief growth and suspension, resting, and buried (“sleeping”) stages (e.g., Davies et al. (1978)). In this classical model, growth occurs at or near measured precipitation rates during these transport episodes. This growth probably does not occur during each transport, but only on rare occasions, such as when an ooid is transported during a warm, sunny afternoon when precipitation rates are highest (Geyman and Maloof, 2019). This hypothesis is supported by aggregated measurements of perceived precipitation rate, which exhibit a log-scaled decrease in apparent precipitation rate with increasing measurement intervals (Fig. 2C). This observation, which is known as the Sadler Effect (Sadler, 1981), is well-documented in systems in which the underlying process is unsteady and intermittent, like sedimentation, erosion, and rainfall rates (Sadler, 1981; Wilkinson, 2015; Schumer and Jerolmack, 2009). Evidence of the Sadler Effect also can be found in the growth rates of other carbonate precipitates, such as speleothems (Fig. 2C).

2. Samples

We measured the shape evolution of ooids from five samples: Great Salt Lake (modern), the Great Bank of Guizhou (Early Triassic), Gatesburg Formation (late Cambrian), Etina Formation (Cryogenian), and the

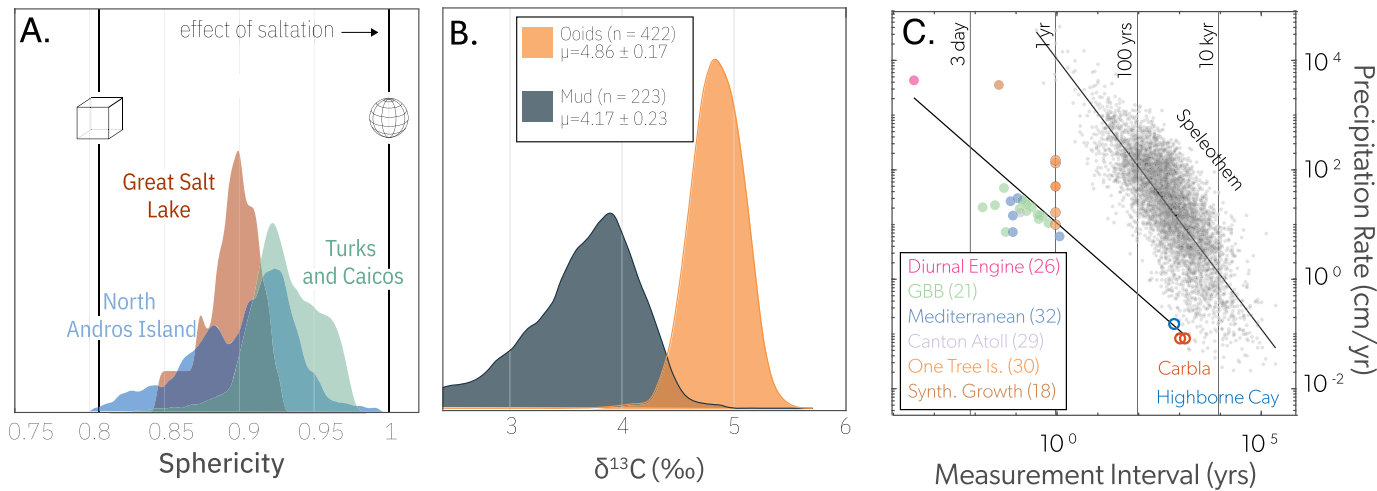


Fig. 2. Previously published data on ooid shape, $\delta^{13}\text{C}$ composition, and the Sadler Effect suggest that abrasion plays a minor role in ooid formation. **A.** The subspherical shape of modern ooids from Andros Island (The Bahamas), Great Salt Lake (USA), and Turks and Caicos (Trower et al., 2018; Jamison-Todd et al., 2020) suggest low abrasion rates. **B.** Ooids and carbonate mud from Andros Island have distinct $\delta^{13}\text{C}$ compositions (Geyman et al., 2022). A two-sample Kolmogorov-Smirnov test rejects the null hypothesis that the ooid and mud samples come from the same distribution ($\text{ks2-stat: } 0.98$, $p\text{-value } << 0.05$). **C.** Measured aragonite precipitation rates have a negative power law dependence on the measurement interval. Therefore, we suspect that the apparent slow growth rates of ooids is a function of the longer ^{14}C measurement interval, not abrasion. Precipitation rate data from Ferguson et al. (1978); Broecker and Takahashi (1966); Smith and Pesret (1974); Davies and Kinsey (1977); Geyman and Maloof (2019); Bialik et al. (2022). This negative power law relationship exists in other settings of carbonate precipitation, like speleothem growth. Speleothem growth data from Comas-Bru et al. (2020).

Matheos Formation (Tonian) (Fig. 3A–E). We specifically chose these samples for their prominent growth rings, which are visible in reflected light and capture a range of sizes from 200 μm to 10 mm, spanning a broad geological timeframe from the Tonian Period to the Recent. Other samples were considered, but the preservation of their laminations was not sufficient for 3D reconstructions of growth history. All of these samples represent ooids that formed in shallow, aqueous environments; for stratigraphic and environmental information about each sample, see SI Appendix.

3. Methods

3.1. Image acquisition

Some minerals and elements have unique reflective characteristics that only can be assessed with light outside the visible spectrum (Kruse, 1996). For example, oxides and clays are apparent in infrared, while phosphorous-bearing minerals fluoresce in UV. For this study, we explored ooid lamination under nine distinct wavelengths, which include: fluorescence from UV (365 nm), blue (470 nm), cyan (505 nm), green (530 nm), yellow (590 nm), red (625 nm), red-edge (730 nm), and two near-infrared wavelengths (760 and 940 nm). For a comprehensive description of the multispectral imaging system, see Manzuk et al. (2022). To optimize computational and storage efficiency, we selected the 4–5 wavelengths that captured the most contrast between growth laminations so we could identify as many growth laminations as possible (SI Appendix Fig. B.10).

We then made 3D reconstructions using the Grinding, Imaging, and Reconstruction Instrument (GIRI) at Princeton University. Using GIRI, we ground 20 μm from the surface of the sample and captured images at the selected wavelengths, each with a resolution of 3.75 μm per pixel. We repeated this process until we were left with a high-resolution stack of photographs. For a complete description of the grinding and imaging process, see Mehra et al. (2022).

3.2. Building 3D models of ooid laminations

Two-dimensional measurements of grain cross-sections can introduce imprecision and inaccuracy, potentially obscuring even large mor-

phological differences (Howes et al., 2021). To mitigate this problem, we constructed a 3D model for each ooid lamination by tracing the lamination in multiple images. For the smallest ooids, we traced the lamination on every image. For the largest giant ooids, there is 100 μm in the z-direction between traces. We generated a triangulated surface from the traces using a standard marching cube algorithm (Lorensen and Cline, 1987). We repeated this process for each visible growth band in an ooid, for at least 10 ooids per sample. We then exported each trace as a point cloud, $y_i = y_i(r, \theta, \phi)$, and fitted a surface to the point cloud using a truncated spherical harmonic series. Each series describes the 3D shape of the growth lamination at a given time. The difference between successive growth laminations describes the shape of the increment of growth.

3.3. Spherical harmonics

The measured surface area of an object with a spherical or ellipsoidal macroscopic shape, but with micro-scale irregularities (like an ooid), will strongly depend on the resolution of the measurement, with higher resolution measurements resulting in larger surface areas (Mandelbrot, 1967). Measuring surface area on the triangulated mesh also is subject to this scale-dependency problem. One solution to this problem is to measure the best-fit ellipsoid. However, an ellipsoid is not a good approximation of the shape of all ooids—particularly those with irregular nuclei like fractured shells or angular quartz grains. We instead use a truncated spherical harmonic (SH) series to characterize the shape of the ooid. The SH series is an effective compromise between a hyper-detailed triangulated mesh (which is still subject to scale-dependency concerns) and an oversimplified best-fit ellipsoid.

To build a surface with SH, we started by normalizing each growth band so that radius of the longest axis is one, which isolates changes in shape by removing the influence of size. Then, we fitted a SH series to the surface of each growth band by placing a fixed point, O , at the 3D centroid of the growth band. The centroid represents the origin of a spherical polar coordinate system where θ is the colatitude, ϕ is the longitude, and r is the distance from the origin, O , to a point on the surface. The functional form of the surface is approximated by:

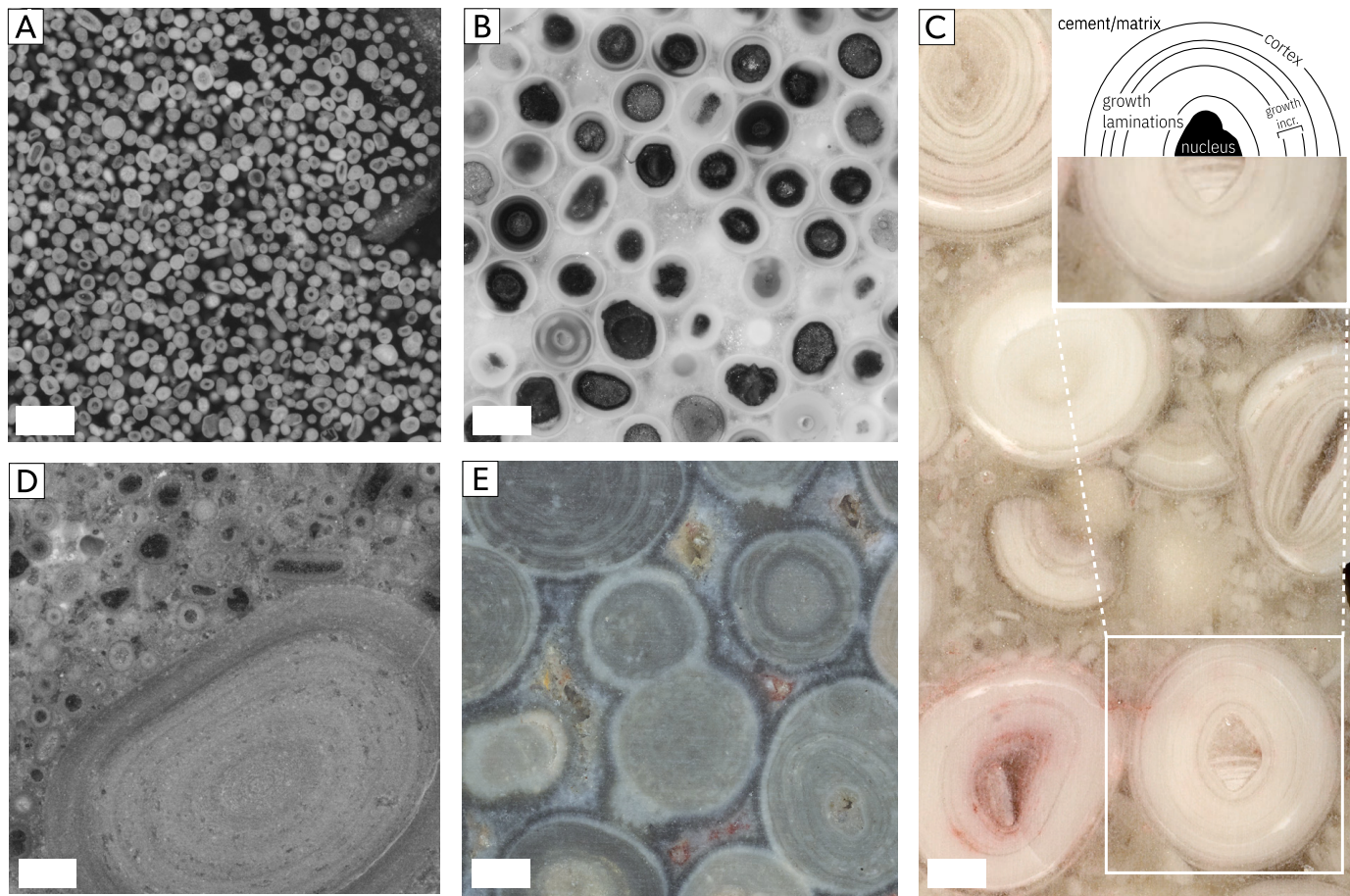


Fig. 3. Samples analyzed in this study. All scale bars are 1 mm. Ooids from **A)** Great Salt Lake State Park, Utah. **B)** upper Cambrian Gatesburg Formation in Pennsylvania. **C)** Lower Triassic Great Bank of Guizhou in southern China. **C-inset** This ooid from the Great Bank of Guizhou contains a nucleus, several visible growth laminations, and is surrounded by cement and matrix. A growth increment is the space between growth laminations. The cortex is the outer layer of the ooid at a given time. **D)** Cryogenian Etina formation in South Australia. **E)** Tonian Matheos Formation in Ethiopia.

$$r(\theta, \phi) = \sum_{l=0}^{l_{\max}} \sum_{m=-l}^l a_{lm} Y_{lm}(\theta, \phi), \quad (1)$$

where a_{lm} is the coefficient determined by least-squares inversion and Y_{lm} is the spherical harmonic, at degree l and order m . As the maximum spherical harmonic degree approaches infinity, $l_{\max} \rightarrow \infty$, the approximation becomes ever more detailed. For shapes like ooids, only a few terms are necessary to accurately describe the surface in a manner that is both more accurate than a fitted ellipsoid and less complex and potentially distorted than a triangulated mesh. We measured the accuracy of the spherical harmonic description by calculating the ℓ_2 -error:

$$\ell_2\text{-error} = \sqrt{\frac{1}{N} \sum_{i=1}^N (y_i - r_i)^2}, \quad (2)$$

where y is a point on the surface of the ooid, r is the spherical harmonic approximation of the surface of the ooid from equation (1), and N is the number of points in the point cloud. We set $l_{\max} = 7$ because there is a rapid reduction in the ℓ_2 -error as l_{\max} increases from 1–5, then slower convergence towards zero past $l_{\max} \approx 6$. Additionally, the terms become less stable as $l_{\max} \rightarrow 15$. To obtain a rotation-invariant shape feature, $L(l)$, we summed the absolute values of all orders (m) of each degree (l):

$$L(l) = \sum_{m=-l}^l |a_{lm}| \quad (3)$$

We used this rotation-invariant shape description to reconstruct the shape of each ooid cortex.

3.4. Forecasting surface-normal growth

Ooid growth occurs by the precipitation of a layer of CaCO_3 onto a nucleus or the cortex of an existing ooid. In a fluid with a uniform solute concentration, mineral precipitation, whether mediated by microbes or abiotic processes, results in growth perpendicular to the surface, known as surface-normal growth (Meakin and Jamtveit, 2010; Sipos et al., 2018). For an ooid, this type of growth is independent of the ooid's fabric, whether it exhibits radial or tangential lamination. Therefore, in the absence of abrasion (e.g., via collisions with other particles or bioerosion), ooid shape would be entirely dependent on surface-normal growth (Fig. 4A). To determine the role of abrasion in the formation of ooids, we model this surface-normal growth and track deviations from the model. To model surface normal growth, we started with a 3D reconstructed ooid cortex and then calculated the surface normal at each vertex on the cortex. Next we grew the ooid along the surface normal vector originating at each vertex, with the amount of growth determined by the maximum thickness of the growth increment (growth increment in the sense of Fig. 3C-inset). We then compared the shape of this modeled ooid to the true, measured shape of the subsequent cortex to understand the influence of abrasion on the ooid shape (Fig. 4D–F). To make this comparison, we calculated the accuracy of the surface normal growth forecast as mean absolute percent error:

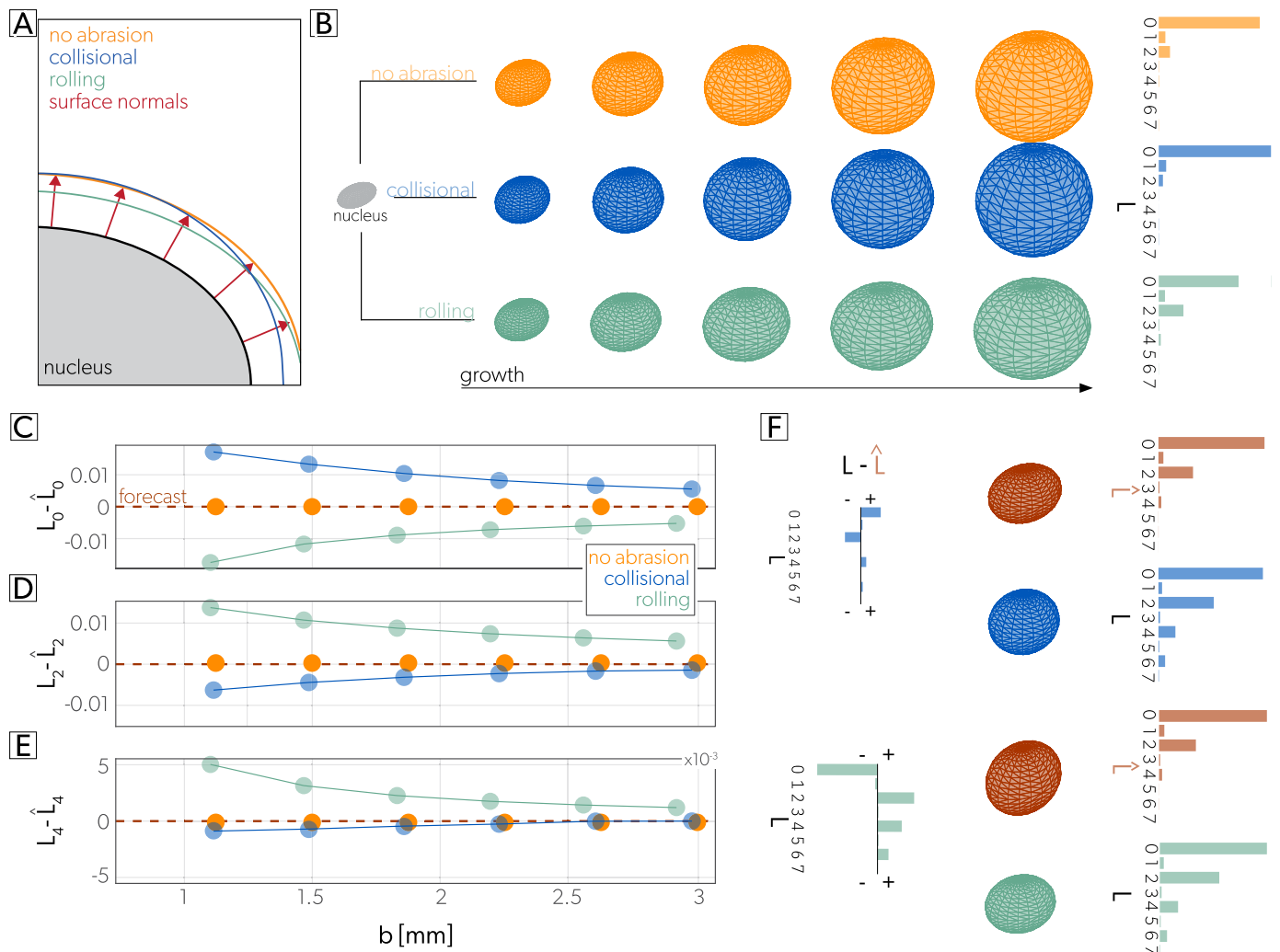


Fig. 4. A visual explanation of the morphological outcomes of abrasion, surface-normal growth model, and spherical harmonics. **A.** We make the forecasted ooid by calculating the surface normal at each point and growing the ooid along that surface normal vector. Collisional abrasion removes excess material from the long axis. Rolling abrasion removes excess material from the short axis. **B.** Three synthetic ooids are grown from an identical nucleus. The ooid in the top row grows in the absence of abrasion, so the shape is entirely controlled by surface normal growth. The ooid in the middle grows via surface normal growth, but with collisional abrasion removing 15% of the added material from the long axis and 1% of the added material from the short axis. The ooid in the bottom row grows via surface normal growth, but with abrasion from rolling, removing 15% of the added material from the short axis and 1% of the added material from the long axis. On the right are the resulting rotationally-invariant spherical harmonic coefficients. This abrasion simulation applies geometric predictions for abrasion based on (Sipos et al., 2018). However, this synthetic experiment only is intended as heuristic since there currently is no model for 3D ooid growth that includes abrasion. **C.** $L_0 - \hat{L}_0$. Collisional abrasion is represented by positive values because the ooid becomes spherical more quickly than expected by surface normal growth. Rolling abrasion is below the forecast because it becomes less spherical than predicted by surface normal growth. **D.** $L_2 - \hat{L}_2$. Rolling abrasion leads to positive values because it is becoming more elongated than predicted by surface normal growth, while collisional abrasion leads to less elongated ooids. **E.** $L_4 - \hat{L}_4$. Rolling abrasion leads to positive values because the L_4 term is required to reconstruct the elongated shape. Collisional abrasion leads to slight negative values because the abrasion produces a more spherical, smooth shape. **F.** A schematic depiction of how $L - \hat{L}$ is calculated for an ooid undergoing collisional abrasion, and one that experiences rolling abrasion. The red ooids are predicted shapes of ooids grown only with surface normal growth (the forecast line from C-E).

$$M = \frac{1}{N} \sum_{i=1}^N \left| \frac{y_i - \hat{y}_i}{y_i} \right|, \quad (4)$$

where y is a point on the surface of the SH reconstruction, \hat{y} is the predicted location of the surface using the surface-normal growth model, and N is the number of points in the reconstruction.

We interpret deviations from the surface-normal growth model, \hat{L} , as contributions from abrasion. Higher L_0 values can be thought of as shapes that are more spherical, higher L_2 can be thought of as shapes that are more ellipsoidal, and higher L_4 values have more bumps on the surface. Collisional abrasion causes positive deviations from \hat{L}_0 , negative deviations from \hat{L}_2 , and closely follows surface-normal growth in \hat{L}_4 . Rolling abrasion leads to negative deviations from \hat{L}_0 and positive deviations from \hat{L}_2 and \hat{L}_4 (Fig. 4d-f). While there currently is no ge-

ometric model for the effects of endolithic borers, we anticipate that they introduce variability primarily to L_4 and higher orders (Mono et al., 2023).

4. Results

Our surface-normal growth model alone predicts 92.7% of the change in L_0 ($1 - M$, from equation (4)). Critically, once a grain becomes a sphere, it is not possible to distinguish between the change in shape from surface-normal growth and collisional abrasion. To ensure that our results are not underestimating the role of collisional abrasion, we held out the most spherical grains. After removing the most spherical grains, the surface-normal growth prediction accuracy continues to explain 93.2% of the signal. The residuals of all samples are

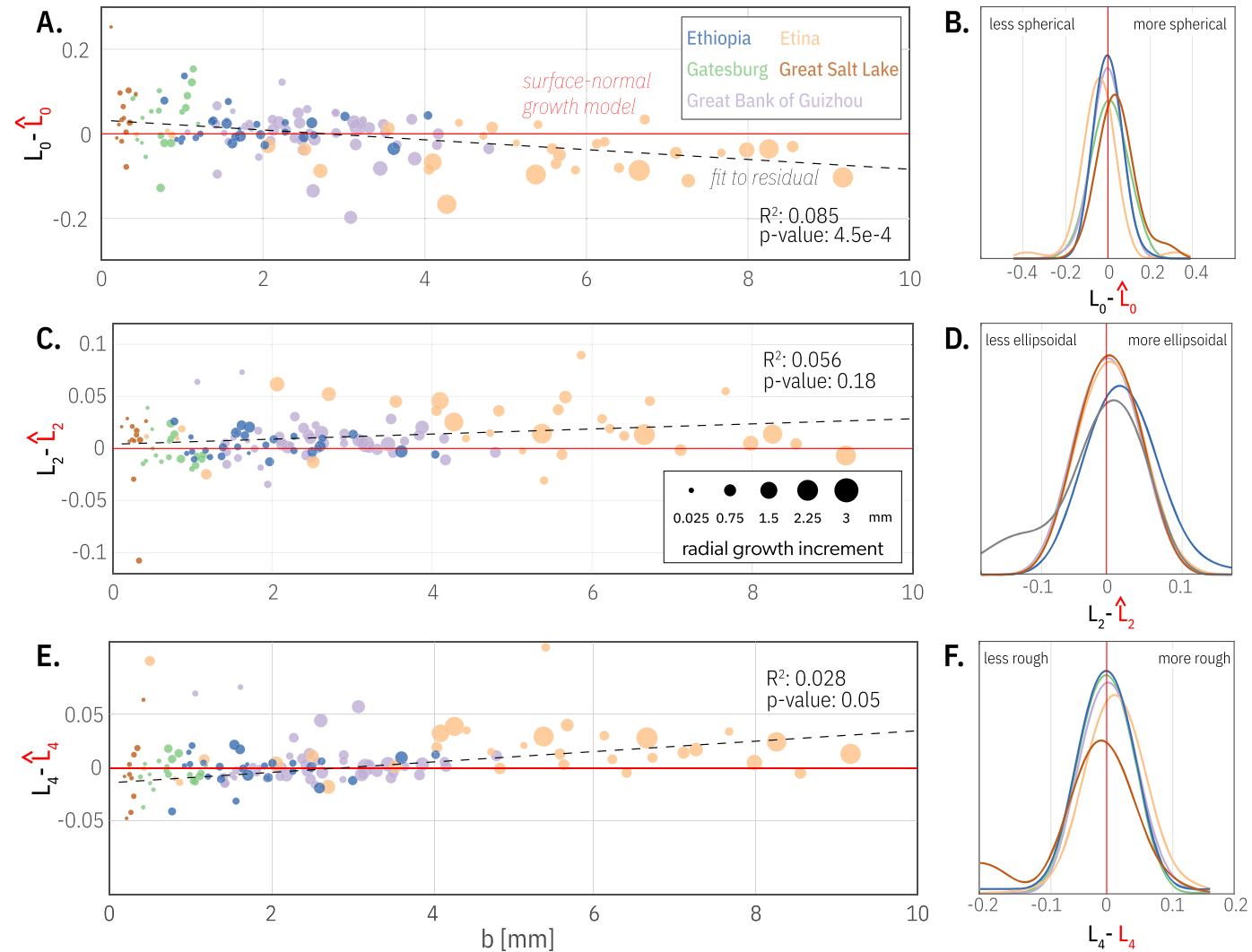


Fig. 5. The comparison of measured ooid growth to the surface-normal growth model. **A.** Surface normal growth alone explains 92.7% of the change in L_0 . **B.** Mean of all residuals is -0.01 . **C.** Surface normal growth alone explains 82.7% of the change in L_2 . Positive values indicate long axes becoming longer than surface-normal growth predicts. Negative values indicate short axes becoming longer than surface-normal growth predicts. **D.** The residuals of the giant ooid samples have means that are very slightly positive, which suggest that surface normal growth does a good job explaining the change in shape, but there is a small contribution from rolling or sliding. The mean of the Gatesburg residual is very slightly negative, suggesting it is becoming a bit more spherical than surface-normal growth predicts. **E.** Surface normal growth alone explains $\sim 55\%$ of the change in L_4 . Positive values represent more bumps and unevenness in the surface texture. Negative values represent smoother surfaces. **F.** The mean of all residuals is centered on zero. There are a couple of outliers from the Great Bank of Guizhou, likely because many of those ooids broke leaving sharp edges susceptible to fragmentation (Fig. 3B).

centered around zero and normally distributed, which suggests that the surface-normal growth model accurately describes the change in L_0 as ooids grow. A linear fit to $L_0 - \hat{L}_0$ (the residual of the surface-normal growth model) would indicate a consistent contribution from abrasion. The linear model of the residuals predicts positive deviations from the surface-normal growth model at small diameters, and negative deviations at large diameters, which suggests that small ooids are more likely to experience collisional abrasion, and large ooids are more likely to roll. While the linear model fit to $L_0 - \hat{L}_0$ is statistically significant ($p << 0.005$), the low R^2 (0.085) of the fit and the normal distribution of the residuals indicate that the surface-normal growth model accurately describes trends in ooid growth morphology (Fig. 5A–B).

The second degree of the SH series, L_2 , represents the best-fit ellipsoid and, therefore, provides a more sensitive indication of changes in grain ellipticity. Surface normal growth predicts 82.7% of the change in L_2 . When we look at $L_2 - \hat{L}_2$ for the Gatesburg sample, the residuals are centered around zero and even slightly negative, which suggests that a combination of surface normal growth and collisional abrasion best ex-

plain the change in shape. The mean of the $L_2 - \hat{L}_2$ residual of all the giant ooid samples are positive, which indicates that giant ooids likely were abraded by rolling (and still did not abrade much) (5C–D). There is not a statistically significant linear fit to the residual ($p = 0.18$, $R^2 = 0.056$), which again suggests that abrasion is not an important process in shaping these ooids.

L_4 represents changes in the roughness of the grain surface. Surface normal growth explains 55.1% of the change in L_4 , and the residuals are centered around zero for all the samples. The synthetic experiments in Fig. 4E demonstrate that collisional abrasion results in small, negative deviations from the surface normal growth model, while rolling abrasion results in larger positive deviations. Additionally, some of the variance could be attributed to microbial and fungal borings adding roughness to the surface of the ooid (Mono et al., 2023). A linear regression of all the residuals demonstrates that when ooids are small, they have slightly negative deviations from the surface normal growth model, consistent with saltation. As the ooids become larger, the devi-

ation becomes positive, consistent with rolling. As with L_0 , the p-value of the residual fit is small (0.05), but so is the R^2 (0.028).

5. Discussion

Based on these 3D reconstructions of ooid growth laminae, we suspect that, to paraphrase Ager (1973)'s comments on the stratigraphic record, an ooid's lifespan may be long yet largely uneventful. Ooids spend most of their time buried, resting on the seafloor, or even saltating, but neither precipitating nor abrading. This view of ooid formation is in agreement with classical models of ooid growth (e.g., Davies et al. (1978)), and is compatible with the existing gross morphology, geochemical, and carbonate precipitation data (Fig. 2). We now transition to examining the implications of this view of ooid formation through a few vignettes that harmonize observations of ooid distribution, abundance, and size.

5.1. What do our data imply for estimates of abrasion rates?

Utilizing ooid size as a proxy for seawater chemistry hinges on properly understanding abrasion rates. Previous studies have used a dynamic equilibrium model of ooid growth to relate ooid morphology to the chemical conditions in the ocean (Trower, 2020; Li et al., 2021). In this model, as an ooid gets larger, the precipitation rate of CaCO_3 increases as a function of the ooid's surface area, but the abrasion rate increases as a function of the ooid's mass, which scales with volume. In theory, with important assumptions about transport intermittency and bed shear velocity, ooid size provides a direct record of parameters like the saturation state of CaCO_3 . Unfortunately, this dynamic equilibrium model was calibrated with the expectation that abrasion, and not episodic precipitation, is responsible for the slow net growth rate of ooids estimated by ^{14}C (Fig. 2C).

Since we have shown that abrasion is not a substantial negative feedback on ooid size, chemical conditions of the ocean likely are the controlling variable for ooid formation. Previous work has demonstrated that the geographic distribution of abiotic carbonate, like mud and ooids, is controlled by source water alkalinity (Geyman et al., 2022). We explore this idea by comparing ooid size and geographic distribution during two periods of Earth history with distinct seawater alkalinity: the Recent and the Last Glacial Period (LGP).

5.2. Ooids in the Last Glacial Period vs. modern ocean

If ooid formation is acutely sensitive to seawater chemistry as we suggest, there should be a discernible difference in the geographic distributions of ooids between the LGP and today. Today, ooids only form in a few oceanographically unique locations (Fig. 6A). What these regions have in common is high alkalinity, with the average alkalinity in ooid-forming regions being in the 99th percentile of tropical–temperate oceans (Geyman et al., 2022) (Fig. 6C). Therefore, we use alkalinity rather than carbonate saturation as a predictor for ooid formation. Alkalinity more accurately reflects the available capacity for carbonate precipitation, given that local processes like photosynthesis or microbial activity can transiently elevate carbonate saturation in many locations, but the amount of carbonate precipitated is limited by the alkalinity. Notably, ooid locations are focused in the Caribbean with minor occurrences in the Persian Gulf, but are nearly absent from the Pacific and Indian Oceans, a phenomenon previously called “the oolite problem” (Milliman, 1969). This strong geographic pattern, coupled with the realization that abrasion plays only a small role in ooid growth, prompts an exploration of historical ooid distribution trends, particularly during different climate epochs, to understand how ooid distribution may represent changes in ocean chemistry.

The increased alkalinity during the LGP led to ooid formation on almost every tropical platform (Fig. 6B), with large ooid depocenters even

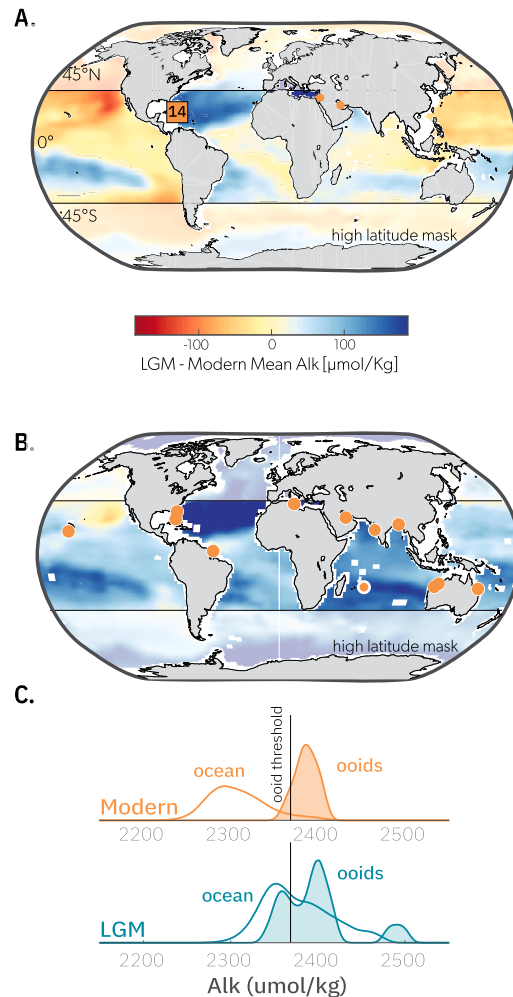


Fig. 6. Alkalinity controls the distribution of ooids in the modern and during the Last Glacial Period. **A.** Deviation from mean alkalinity in the modern ocean with ooid occurrences labeled. Alkalinity measurements from the GLODAP Dataset (Key et al., 2004). **B.** Deviation from the modern mean alkalinity value during the Last Glacial Maximum, with the location of ooids dating from 120–10 Kyr. Alkalinity values are from the Institut Pierre-Simon Laplace (IPSL) CM5A Earth system model in which sea level is 116 m below the pre-industrial level. For more information on the IPSL CM5A model parameters, see Kageyama et al. (2013). **C.** The average alkalinity of the source water for modern ooid-forming environments is in the 99th percentile of the ocean excluding the poles. An increase in global alkalinity causes the average alkalinity of the Last Glacial Maximum ocean to be near the threshold for ooid formation, leading to more broadly distributed ooids during the Last Glacial Maximum.

found throughout the Indian and Pacific Oceans (Milliman, 1969; Gallagher et al., 2018; Rao, 1964). Compared to the modern ocean, with isolated ooids only forming due to special oceanographic conditions, the expansion of ooid-forming environments during the LGP demonstrates the sensitivity of ooid formation and abundance to changes in alkalinity. Additionally, ooid localities from the LGP are now ≈ 100 m underwater, so they are almost certainly undersampled, meaning that ooids likely are even more abundant and widely distributed during the LGP than we currently appreciate. These findings encourage further investigation into how ooid distributions in the past could provide insights into ancient oceanographic conditions.

5.3. The Phanerozoic through the eyes of ooids

There is a long history of using the inferred mineralogy of ooids to reconstruct long-term trends in climate and the chemistry of the ocean

(Sandberg, 1983; Wilkinson and Given, 1986; Opdyke and Wilkinson, 1990). The comparison of the LGP to modern ooid distributions demonstrates that the chemical conditions of the ocean are not just recorded by the mineralogy of ooids, but also by their abundance and geographic distribution.

To demonstrate this point, we analyze two independently constructed records of ooid abundance in the Phanerozoic. The first is ooid occurrences extracted from literature using xDD and assigned ages based on stratigraphic identifiers from Macrostrat (Zhang et al., 2013; Peters et al., 2018, 2017), which limits this dataset to North America (see SI Appendix B.2). We normalize the ooid occurrences by dividing by the total number of carbonate occurrences (also extracted from Macrostrat) to determine the proportion of carbonate occurrences that contain ooids. We then multiply by the total number of carbonates, which amplifies intervals when carbonate environments are abundant and ooids are present in a high proportion of the carbonate occurrences. Due to its proximity to the equator and exceptionally detailed occurrence information in xDD and Macrostrat, North America is an excellent region for studying the abundance and composition of carbonates during the Paleozoic era. To ensure that our dataset is not just representative of North American trends, we compare the xDD dataset to a global database of allochemical composition of Phanerozoic carbonate platforms (Kiessling et al., 2003). These two datasets contain the same broad trends in ooid abundance (Fig. 7A).

We suggest that the Phanerozoic record of ooid abundance (Fig. 7A) reflects a Goldilocks problem between abundant carbonate shelf area and favorable seawater chemistry for ooid formation. On one hand, increasing the total area of shallow-water carbonates should lead to a proportional increase in the number of ooid occurrences. However, this zeroth-order prediction is complicated by the feedback whereby increased carbonate shelf area increases the carbonate sink, acting to decrease the ocean's carbonate saturation state and alkalinity (Opdyke and Wilkinson, 1988; Opdyke and Walker, 1992), which disfavors ooid production. This mass balance can be illustrated with a simple one-box model of the ocean's carbonate budget (Fig. 7D). Let the influx of dissolved inorganic carbon (DIC) and alkalinity to the ocean remain constant through time. The dominant sink of carbon and alkalinity is from carbonate precipitation, represented as:

$$F_{\text{out}} = A_{\text{shallow}}(\Omega - 1)^n + F_{\text{deep}}, \quad (5)$$

where F_{deep} represents the flux of alkalinity to the deep marine sink, which substantially increased following the Mid Mesozoic Revolution (Ridgwell, 2005). A_{shallow} is the area of shallow-water carbonates, and $(\Omega - 1)^n$ is the canonical carbonate precipitation rate law (Burton and Walter, 1987). As A_{shallow} increases, the steady-state Ω must be lower for the ocean to maintain constant carbonate outflux. Importantly, Ω depends not only on seawater carbonate chemistry, but also major ion composition (Zeebe and Tyrrell, 2019). Specifically, since Mg^{2+} hinders the activity of the CO_3^{2-} anion, increasing the seawater Mg/Ca leads to a decrease in Ω for the same alkalinity (Zeebe and Tyrrell, 2019). Thus, periods with high seawater Mg/Ca can maintain higher alkalinity even when the carbonate shelf area is large, providing an opportunity to optimize the Goldilocks conditions for maximum ooid occurrences. Our model is agnostic to the precise mechanism that controls the major ion composition of seawater (Berner, 2004; Dunlea et al., 2017).

Using estimates of the Phanerozoic shallow tropical shelf area and seawater Mg/Ca (Figs. 7B–D), we construct a zeroth-order model for ooid abundance. In each timestep, we use mass balance and equation (5) to update the ocean's carbonate system parameters (alkalinity, DIC, Ω). We predict that relative ooid abundance in each timestep is the product of the total area of tropical shelves and the ocean's alkalinity.

Our zeroth-order model broadly matches ooid abundance records from the Phanerozoic (Fig. 7E). The model exhibits an $R^2 = 0.61$ when evaluated against the xDD dataset, with a p-value << 0.05. When eval-

uated against the allochemical dataset, the model has an $R^2 = 0.32$ and a p-value << 0.05. To ensure that the correlations between the ooid potential model and the datasets are robust, we compared the model fit to 50,000 random models. The ooid potential metric exhibits a stronger correlation with the xDD dataset than any of the randomly generated time series and is in the 92nd percentile when compared to a randomly generated time series with the same time bins as the allochemical dataset.

Next, we examine a few vignettes to illustrate how this zeroth-order ooid potential model can help us make sense of how changes in seawater chemistry influenced ooid distributions in the Phanerozoic. By the mid-Cambrian-Early Ordovician, the Sauk transgression had flooded the continents, leading to increased shelf area (Peters and Gaines, 2012). Without abundant coral reefs and other large calcifying organisms, which had not yet proliferated (Pruss et al., 2010; Rowland and Shapiro, 2002), the primary sink for alkalinity was abiotic precipitation of $CaCO_3$, which can be seen in the high normalized ooid occurrences, and in the broad geographic distribution of ooids in the Late Cambrian (Figs. 7A&F). Continued high shallow shelf area combined with the evolution of metazoan calcifiers likely lowered the alkalinity of Late Ordovician to end-Devonian oceans, leading to fewer ooids and a narrowed geographic distribution of ooids reminiscent of the provincial ooid depocenters of the modern ocean (Fig. 7G). The Late Devonian extinction was especially devastating to reef-builders, causing the extinction of stromatoporoid sponges and the collapse of tabulate reef ecosystems (Yao et al., 2020). With a reduction in calcifying organisms, alkalinity rose, which led to an increase in the abundance of ooids through the early Carboniferous. Normalized ooid abundance remains high during the early portion of the Late Paleozoic Ice Age (LPIA) despite declining shelf area, as glacioeustasy, rising Mg/Ca, and the slow recovery of metazoan reefs sustained high alkalinity.

The success of this zeroth-order ooid potential model highlights the connection between ooid abundance and seawater chemistry, prompting a closer examination of changes in ooid size through the Phanerozoic.

5.4. Does ooid size reflect seawater chemistry?

Ooid size also has been proposed as a marker of ancient seawater chemistry (Trower et al., 2017; Trower, 2020; Koeshidayatullah et al., 2022). Our finding that abrasion has only a minor impact on ooid growth suggests that abrasion is not an important negative feedback mechanism on ooid size (see Fig. 5). As a result, ooid size may be more strongly influenced by chemical conditions in the ooid-forming environment than previously believed. This notion is supported by a weak correlation between ooid diameter and alkalinity in ooids from the modern and LGP ($R^2 = 0.46$, p-value = 0.09) (Fig. 8A).

Admittedly, ooid size data for modern and the LGP are sparse. However, if our hypothesis about the effect of alkalinity on ooid distribution and size is correct, we expect that when alkalinity increases, ooids will form in more locations and the median size of ooids should increase. Ooid size, being substantially influenced by local environmental factors, results in a wide range of sizes within any single time period; however, our objective is to see through this environmental noise and determine if changes in the average ooid size through time are indicative of shifts in global alkalinity. We test for this expectation using an existing database of ooid sizes (Koeshidayatullah et al., 2022). To account for the errors associated with 2D measurement, we build a new distribution of ooid sizes for each period, leveraging the assumption that the true minor axis length of each ooid could be underestimated by up to 20% (Howes et al., 2021). We compare the resampled size distributions to the proportion of ooid occurrences (derived from xDD data) per time period (Fig. 8B; see SI Appendix B.3).

Through this comparison, we find that there is a statistically significant correlation between the minor axis length and the number of normalized ooid occurrences ($R^2 = 0.62$, p-value = 0.0025). In other

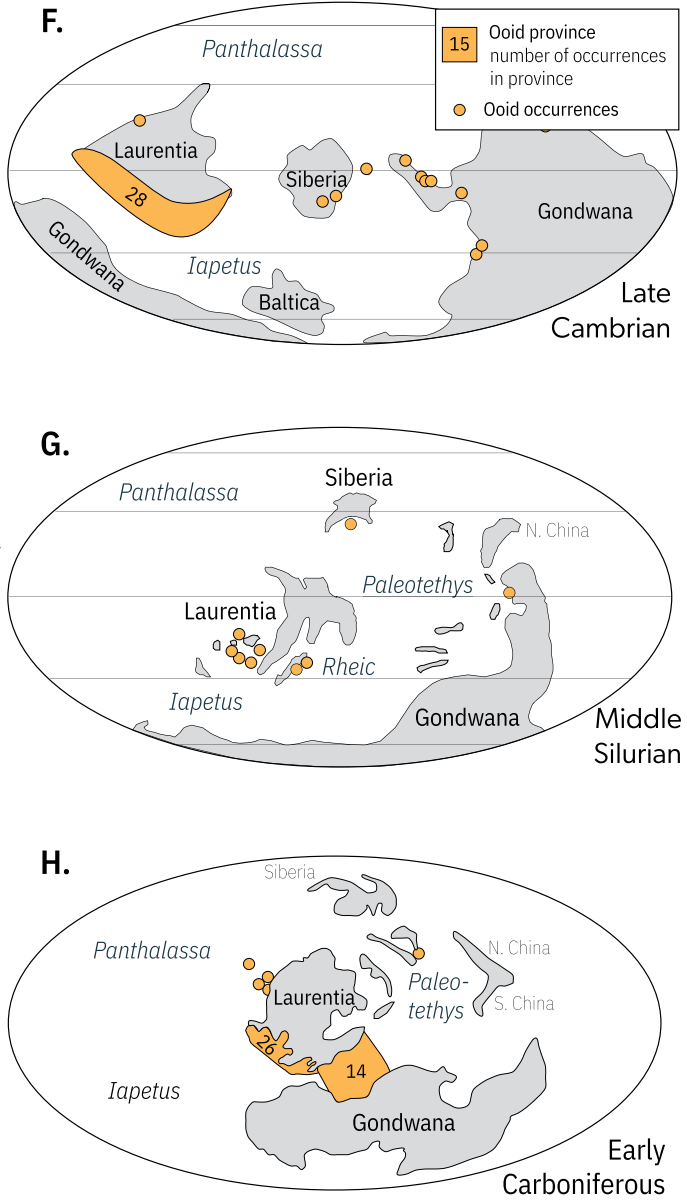
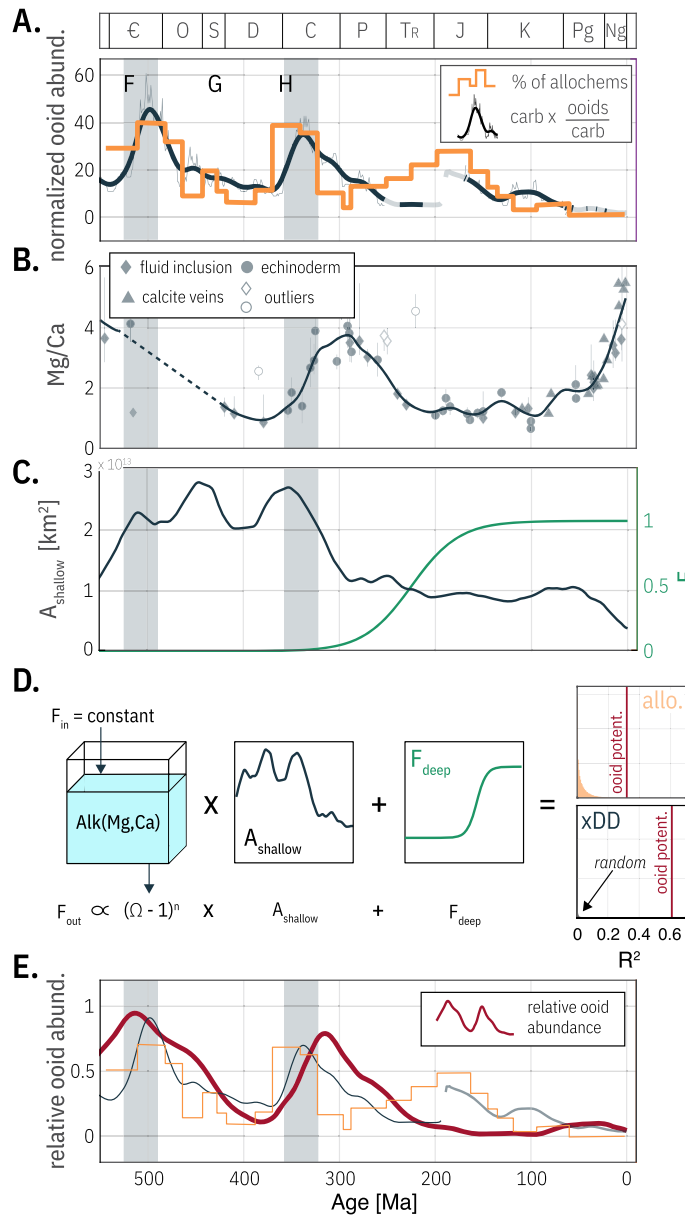


Fig. 7. An ooid potential model can explain the abundance of ooids throughout the Phanerozoic. **A.** Normalized ooid occurrences through the Phanerozoic. To normalize the occurrences extracted from xDD, we calculate the proportion of ooid occurrences among all carbonate occurrences of the same age. We then multiply this proportion by the total number of carbonate occurrences of the same age, giving us the normalized count of ooid occurrences. The percent of allochems is based on the estimates of allochemical compositions (Kiessling et al., 2003). **B.** Variations of Mg/Ca of the ocean throughout the Phanerozoic (Ries, 2010; Rausch et al., 2013; Gothmann et al., 2015; Coggon et al., 2010; Dickson, 2002). **C.** Changes in tropical, shallow-water shelf area through the Phanerozoic estimated with (Blakey et al., 2008; Blakey and Ranney, 2017), and a simplified evolution and proliferation of planktonic calcifiers modeled as a sigmoid function (Martin, 1995). **D.** Schematic illustration of the ooid potential model and distribution of R^2 for comparing randomly generated time series to the ooid potential model. The ooid potential model outperforms all randomly generated time series for the xDD dataset and is in the 92nd percentile for the allochemical dataset. The allochemical dataset has fewer data points than the xDD dataset, so it is more likely for a randomly generated time series to be highly correlated. **E.** The ooid potential model (eq. (5)) compared to xDD and the allochemical dataset. **F.** Ooids were abundant and globally distributed during the Late Cambrian, which suggests elevated alkalinity. **G.** During the mid-Silurian, ooids were sparse and geographically isolated to the southern margin of Laurentia. **H.** During the early Carboniferous, ooids were abundant in the shallow-water tropics, with many occurrences on the southern margin of Laurentia and in the narrow sea forming between Gondwana and Laurentia.

words, the conditions that lead to the highest number of normalized ooid occurrences also lead to the largest ooid sizes (Fig. 8C). To ensure that this signal is not a function of over sampling of certain periods, we repeatedly subsample the size database, such that the number of unique locations per period is proportional to the ooid occurrences per period. The most positive correlation coefficients also have the most statistical significance, suggesting that this signal is robust (Fig. 8D). The two

periods with the largest median ooid size are the Cambrian and the Carboniferous, which is what we would predict based on the Phanerozoic normalized ooid occurrences and the zeroth-order ooid potential model (Figs. 7A&E). It also is worth noting that three of the four periods with the smallest ooids are in the Cenozoic, well after the Mid Mesozoic Revolution, and the fourth is the Silurian, which had the Paleozoic minimum for normalized ooid occurrences.

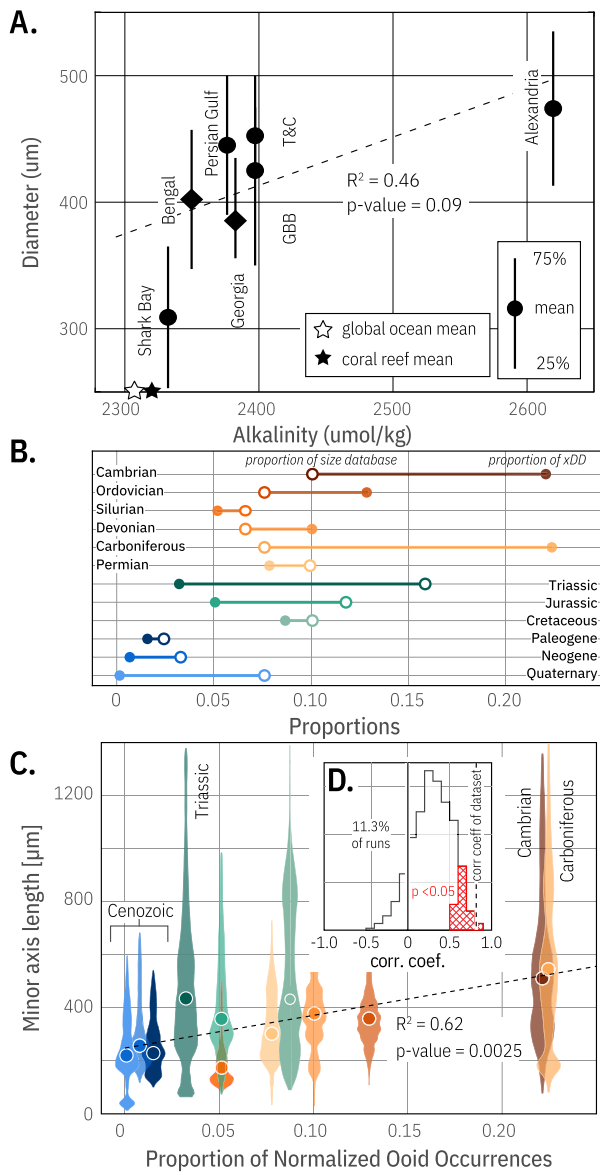


Fig. 8. Higher alkalinity may result in larger ooid sizes in the modern and Phanerozoic. **A.** Diameter of ooids as a function of the total alkalinity of the source waters. The total alkalinity of source waters is from the Global Data Analysis Project (Key et al., 2004). Ooid sizes from Turks and Caicos (Trower et al., 2018), The Bahamas, and Shark Bay were measured with a camsizer. Ooid sizes from the Persian Gulf are from Abu Dhabi Island and measured with a sieve (Loreau and Purser, 1973). Measurements from Alexandria Beach, Egypt were made on photomicrographs from (El-Sammak and Tucker, 2002). Depending on the composition of seawater, as alkalinity increases, the increases in saturation state slow down because of reduced ion activity (Zeebe and Tyrrell, 2019). **B.** To address potential bias from uneven sampling in the database of ooid sizes (Koeshidayatullah et al., 2022), we utilized a resampling approach that adjusted the size database to match the proportions found in the xDD database, using the same weighting scheme as illustrated in (Fig. 7A). **C.** After resampling, we find that there is a statistically significant correlation ($p = 0.0025$) between the abundance of ooids and the median minor axis length of ooids from that period. **D.** To evaluate if the correlation is robust, we ran 1000 simulations, each time randomly selecting locations for each period and drawing ooids from these locations. We calculate the correlation coefficient between the median size and proportion of normalized ooid occurrences. We get a range of correlation coefficients, but only strong, positive correlations have statistically significant p-values.

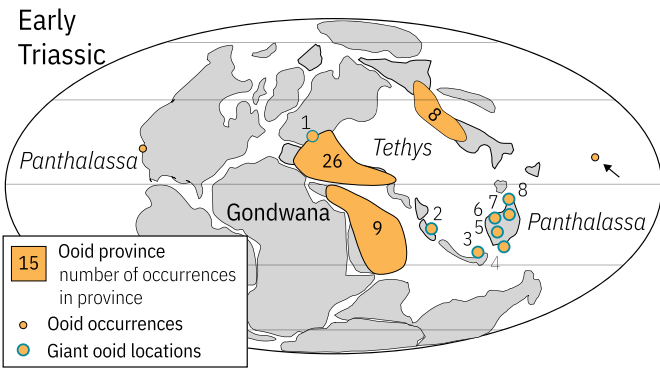


Fig. 9. Ooids and giant ooids are abundant in the Tethys, but relatively scarce in Panthalassa. Figure is modified from (Li et al., 2015). The provinciality of the ooid distribution during the Early Triassic bears more similarity to the distribution of ooids today, a world with overall low alkalinity, but with localized regions of high alkalinity and abundant ooids (Fig. 6A).

5.5. What are the implications for the formation of giant ooids?

The presumption of high abrasion rates in the current formulation of the dynamic equilibrium model has led to two families of hypotheses about the formation of giant ooids: (1) very high precipitation rates from unrealistic ocean chemistries to overcome increased abrasion as the mass of the ooid increases (Trower, 2020), and (2) decreased abrasion rates by altering seawater chemistry enough to create viscous dampening of ooid collisions or allowing ooids to grow while buried (Simpson, 2021; Anderson et al., 2020). But, if abrasion rates are low, as we have shown with 3D models of ooid growth laminae, a relatively small increase in the longterm precipitation rate can result in the formation of giant ooids, and mechanisms to shield giant ooids from abrasion are not required. Additionally, local conditions can amplify global alkalinity, leading to larger ooid sizes.

For example, the abundance of ooids, and particularly giant ooids, during the Early Triassic has led researchers to hypothesize that the scarcity of animals that produce skeletal carbonate immediately following the end-Permian mass extinction led to extremely high saturation state in the ocean (Li et al., 2021; Payne et al., 2006b), which may be true. But these hypotheses do not account for the strong provincialism of Early Triassic ooid occurrences (Fig. 9), which are almost entirely focused in the Tethys Ocean. The geographic distribution of ooids in the Early Triassic looks more similar to the modern, provincial distribution than the more broadly distributed ooids during LGP (Fig. 6D).

There were almost certainly some extreme conditions in the Early Triassic ocean due to the effects of extinction and the eruption of the Siberian Traps. However, extrapolating from the Tethys to the global ocean in the Early Triassic potentially is similar to expecting an oceanographically unique place, like The Bahamas, to be representative of the global ocean today. The lack of a global distribution of Early Triassic ooids suggests global alkalinity was not exceptionally high.

Instead, the Tethys was a unique embayment with oceanographically amplified alkalinity. In fact, throughout the early Mesozoic, the ooid potential model diverges from the normalized ooid occurrences (Fig. 7E). This discrepancy may be due to unfavorable global conditions for ooid formation, while the Tethys behaved like an even more intense modern-day Caribbean, amplifying regional alkalinity and producing ooids. Therefore, the end-Permian extinction probably did increase global alkalinity enough to make Tethyan ooids transiently bigger and more abundant, but not enough to cover the world in ooids.

6. Conclusions

The simple presence of ooids imposes a constraint on seawater chemistry and hydrodynamic conditions, indicating that the saturation

state of water has exceeded the threshold for carbonate precipitation and that the location is above wave base. Modern and LGP ooids demonstrate that increasing alkalinity locally leads to an increase in ooid size. An increase in mean alkalinity (like during the LGP) also leads to a broader geographic distribution of ooids. These lessons about the effects of alkalinity and the distribution and size of ooids provide new tools for using the presence, abundance, and size of ooids as paleoenvironmental proxies. This new appreciation for the meaning of abundance, geographic distribution, and size of ooids is possible because of the improved understanding of ooid formation from 3D models of ooid growth, the realization that abrasion rates are low, and the recognition of the Sadler Effect in ooid growth rates. Future work incorporating the role of paleobiology in the formation and erosion of ooids will allow us to use ooids not just as a record of seawater chemistry, but also as a record of microbial communities throughout Earth's history.

CRediT authorship contribution statement

Bolton Howes: Conceptualization, Data curation, Formal analysis, Investigation, Methodology, Validation, Visualization, Writing – original draft, Writing – review & editing. **Akshay Mehra:** Data curation, Formal analysis, Methodology, Writing – review & editing. **Emily Geyman:** Data curation, Formal analysis, Methodology, Writing – review & editing. **Julia Wilcots:** Data curation, Methodology, Writing – review & editing. **Ryan Manzuk:** Data curation, Methodology, Writing – review & editing. **Curtis Deutsch:** Data curation, Methodology, Writing – review & editing. **Adam Maloof:** Conceptualization, Methodology, Writing – original draft, Writing – review & editing.

Declaration of competing interest

The authors declare that they have no known competing financial interests or personal relationships that could have appeared to influence the work reported in this paper.

Data availability

The link to the data repository: <https://data.mendeley.com/datasets/3zpj3bd5w4/1>.

Acknowledgements

We thank I. Buynevich and A. Balzani for use of the camsizer. A. Krokchine and E. Cano assisted data collection. F. Simons assisted with spherical harmonic analyses. J. Husson for his help with xDD. M. Nadeau provided geochemical insights. This manuscript is much improved based on the thoughtful reviews of L. Kah, A. Immenhauser, two anonymous reviewers, and the editor, H. Bao. S. MacLennan, C. Rose, J. Strauss, S. Edmonson, D. Lehrmann and N. Anderson provided samples. We thank D. Jerolmack, G. Domokos, and A. Sipos for discussions about abrasion and 3D geometry. This work was supported by NSF Earth Sciences Grant 1028768 to A. Maloof.

Appendix A. Sample appendix section

A.1. Sample descriptions

A.1.1. Great Salt Lake

The modern ooids of the Great Salt Lake are forming on the wave-agitated shores of the hypersaline lake (Eardly, 1938). The ooids are made of radial aragonite precipitated on nuclei composed of fecal pellets and quartz grains (Fig. 3A; Eardly (1938); Sandberg (1975); Trower et al. (2020)). Ooids from Great Salt Lake have well-preserved laminations because of the absence of microboring Cyanobacteria (Trower et al., 2020). The sample from this study was collected from the beach on

the southern end of the lake in Great Salt Lake State Park (N 40.741°, W 112.205°, WGS84).

A.1.2. Great Bank of Guizhou

The Lower Triassic sediments on the Great Bank of Guizhou in southern China were deposited in the aftermath of the end-Permian Mass Extinction (Fig. 3B). Oolitic units are widespread on the Great Bank of Guizhou, along with lime mudstone (Payne et al., 2006a). The giant ooids commonly are nucleated on the broken cortices of other giant ooids which, along with cross-bedding and planar lamination, suggest deposition in high-energy shoals (Lehrmann et al., 2012). Petrographic studies of the GBG ooids have shown that the growth laminations alternate between micritic layers and layers replaced with coarse, sparry calcite (Lehrmann et al., 2012). The alternating textures have led to the interpretation that the ooids originally were bimimetic, with the micritic layers being calcite and the coarse spar layers are recrystallized from original aragonite (Lehrmann et al., 2012).

A.1.3. Gatesburg

The upper Cambrian Gatesburg Formation in Pennsylvania was deposited on what was the southern margin of Laurentia (Fig. 3C). In outcrop and core from central and western Pennsylvania, ooid grainstone dominates the Gatesburg Formation, leading previous workers to suggest that the ooids formed on a widespread carbonate sand shoal (Laughrey and Harper, 2012). In some locations, the oolitic grainstones of the Gatesburg Formation are laterally and vertically adjacent to meter scale microbial patch reefs (Laughrey and Harper, 2012).

A.1.4. Etina

The Etina Formation in South Australia was deposited during the Cryogenian period between the Sturtian and Marinoan snowball Earth events (Singh, 1987). The oolitic portions of the Etina Formation are interbedded with stromatolitic limestones and intraclast conglomerates, suggestive of occasional subaerial exposure (Rose et al., 2013; O'Connell et al., 2022). The ooids themselves are micritized (Fig. 3D), with iron oxide-rich laminations that make their growth increments easily identifiable (McKirdy et al., 2001). The matrix between the giant ooids is made up of normal-sized ooids, which suggests that giant ooids grew amongst normal-sized ooids or in laterally adjacent environments.

A.1.5. Matheos formation

The Matheos Formation in Ethiopia is late Tonian in age, deposited prior to the Sturtian glaciation (MacLennan et al., 2018; Park et al., 2020). The Matheos Formation contains dark gray-black limestone ribbonite with molar-tooth structures, intraclast breccia, stromatolites, and oolites (Park et al., 2020). The sample in this study was collected east of Zamra Fault (Park et al., 2020), where the Matheos Formation is dominated by alternating oolites and stromatolites (Fig. 3E).

Appendix B. Additional Methods

B.1. Band Selection

To optimize computational and storage efficiency, we select the 4–5 wavelengths that display the most contrast between growth laminations. To choose this subset of wavelengths, we polish the sample flat and take images with all nine available wavelengths (Fig. B.10A) using a Phase One IQ4 150-megapixel achromatic digital back accompanied with a 120 mm Schneider Kreuznach apochromatic macro lens. This imaging setup allows images that are 1:1 (the image of the object projected onto the camera sensor is the same size as the object itself) with a field of view that is 4.04 x 5.37 cm and a resolution of 3.75 μm per pixel. We normalize the exposure across all images (Fig. B.10A-inset histograms) via linear dynamic range expansion. Then, we perform a principal component analysis (PCA) on all the channels (Fig. B.10B–C) to determine which channels explain the most variance in the image.

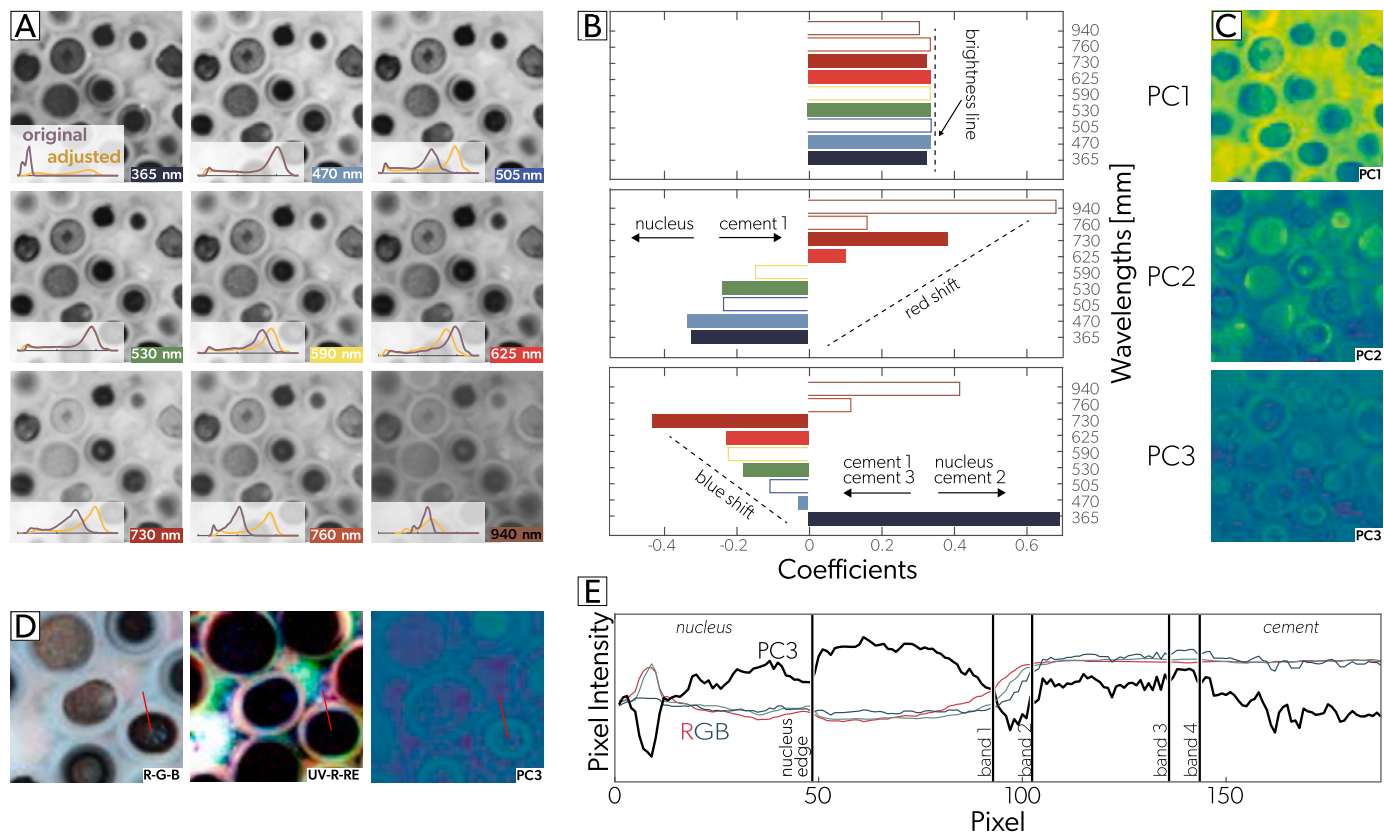


Fig. B.10. A) Images of the Gatesburg oolite in nine wavelengths. The kernel density plots show the distribution of pixel intensities prior to normalization and following normalization. B) The coefficients of the first three principal components that inform which bands we select (those marked with a solid bars). C) Images representing the first three principal components. D) RGB, a false-color image showing UV-R-Red-edge, and PC3 of the selected channels demonstrate how the additional channels enhance the contrast between growth laminations and also between the different phases of cementation. The red line is the transect for pixel values in E. E) The comparison of pixel intensities in RGB versus PC3 of the 5 selected channels depicts how the additional channels make growth laminations easier to detect.

PC1 often represents the brightness of an image (where each channel has the same coefficient; (Fig. B.10C). Next, we choose which channels have the strongest weights in PC2 and PC3. As an example of this selection process, for the Gatesburg oolite we choose 365, 470, 530, 625, and 730 nm. We choose 470, 530, and 625 nm because they are blue, green, and red wavelengths used in traditional RGB photography. The RGB images provide an archive of true color images for human-eye driven descriptive work that can compliment the image processing done in 5D space (Fig. B.10D). We choose 365 nm (UV-fluorescence) and 730 nm (red-edge) because of their strong weights in PC2 and PC3, indicating that these wavelengths explain more of the variance (contrast) in the image than other wavelengths (Fig. B.10D), which aids in the identification of growth bands (Fig. B.10E).

B.2. xDD and Macrostrat data extraction

North American geologic formations containing ooids were identified using literature contained in the xDD corpus and following the methods outlined in Peters et al. (2017), an example of which can be found in the [Macrostrat github repository](#). We first search the xDD corpus of published literature for words (or strings) that indicate ooids (e.g. the string “oolit-” matches “oolitic” and “oolite”). We then match ooids to the geologic formation in which they are found using simple rules: if “ooid” and a Formation Name are found in the same sentence with no negating terms (e.g. “non-”), we assume that Formation contains ooids. After repeating this search over every ooid-Formation pair in the corpus, we cross reference the list of ooid-bearing formations

with North American formations contained in the Macrostrat database ([macrostrat.org](#), Peters et al. (2018)).

Each formation in Macrostrat has been assigned an age using a continuous-time age model based on stratigraphic relationships and radiometric age constraints, which allows us to assign an age (at 1 Myr resolution) to each ooid occurrence we identify. In total, we identified 1172 unique ooid-bearing formations in the North American geologic record.

B.3. Processing the size database

B.3.1. An observed signal

We begin by binning the size data from Koeshidayatullah et al. (2022) by geologic period. We then plot the binned median values versus the number of unique locations per period (here, we consider each distinct outcropping of rock, rather than individual stratigraphic bed, member, or group, as a “unique location”). The result is a weak positive correlation between number of depositional locations and ooid size ($R^2 = 0.28$ and $p = 0.07$; Fig. B.11).

B.3.2. Propagating size error

Size measurements in the database assembled by Koeshidayatullah et al. (2022) were measured on photomicrographs and polished slabs. However, Howes et al. (2021) demonstrated that measurements made on two-dimensional (2D) cross sections tend to underestimate the true axis lengths. To mitigate this error, we focus on minor axis measurements, which exhibit less error when compared to major axis lengths. Still, errors of up to ~20% in minor axis lengths are common when us-

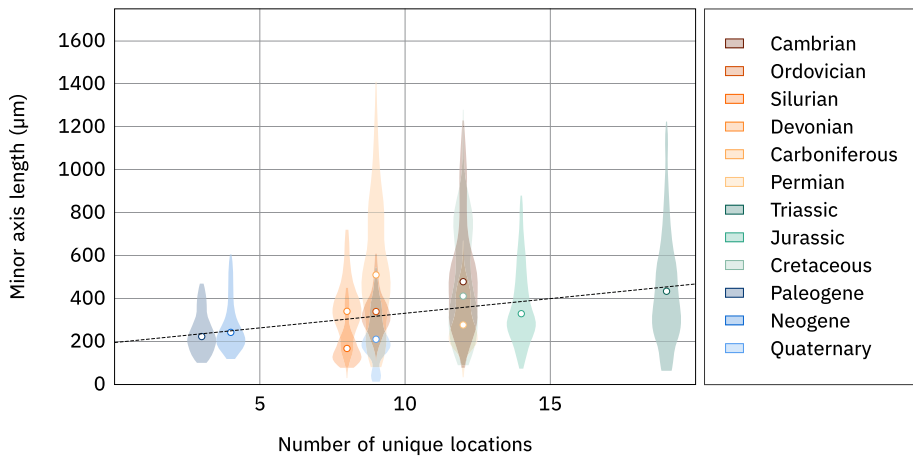


Fig. B.11. Violin plot showing size distributions of ooids versus unique locations as reported in the Koeshidayatullah et al. (2022) database. The dashed line depicts a linear regression.

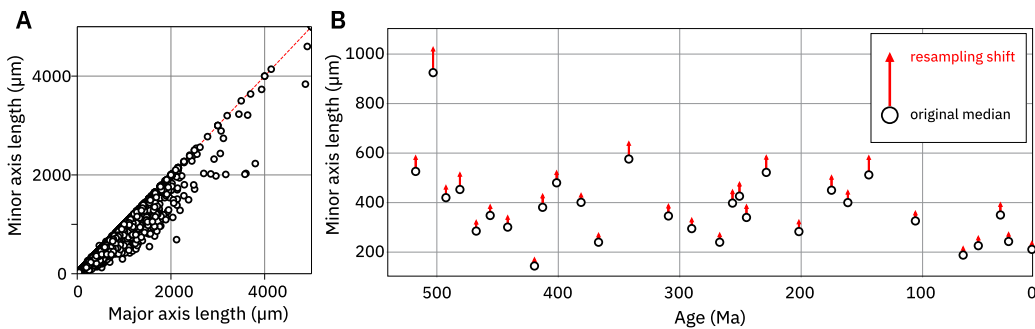


Fig. B.12. A) Minor versus major axis lengths for the ooids in the Koeshidayatullah et al. (2022) database. The dashed red line represents an aspect ratio of 1 (i.e., perfectly circular or, if extrapolated to 3D, perfectly spherical). The ooids in this dataset have a mean aspect ratio of 0.90. B) The effects of error propagation. The empty circles represent the median minor axis length for a given point in time in the Koeshidayatullah et al. (2022) database. The red arrows depict how the median shifts once we complete the procedure described in Section B.3.2 (i.e., the tip of the arrows being the new median value).

ing 2D measurements. To ensure that measurement errors do not affect the observations presented in Section B.3.1, we resample the size data with uncertainty. In the initial step of resampling, we define a minor axis size range for each ooid, x , such that:

$$s \leq x \leq (s * (1 + m)) \quad (\text{B.1})$$

where s is the reported minor axis measurement and m is the maximum error, in percent.¹ We use a error value of 20% for m .

Having defined a size range, we resample the size data n times (here, $n = 1000$). Each time, for x ooid, we draw a new minor axis value (rounded to the nearest whole micron) from a uniform distribution informed by the range in Equation (B.1). Following resampling, we compile all drawn values into a new dataset, D , which we then can use for statistics and further analyses (e.g., Fig. B.12).

B.3.3. An updated signal

Without further analyses, we cannot be sure if this trend solely is a result of the makeup of the Koeshidayatullah et al. (2022) dataset. Ideally, the number of unique locations per period would be proportional to the true accounting of Earth's carbonate (or ooid) system through time.² That is, periods with increased ooid production—whether de-

fined using areal extent, loci of precipitation, or some other metric—would contain more unique locations than periods with reduced ooid production. Likewise, the distribution of minor axis lengths for each geologic period would be representative of the true distribution of ooid sizes during that time (Fig. B.13).³

While enforcing the latter ideal would require many more measurements of ooids (an undertaking that is outside the scope of this paper), ensuring the former can be done using independent records of geology (e.g., Ronov et al., 1980; Peters et al., 2018).⁴ Having explored several such sources (see Table B1), we choose to utilize a record derived from xDD, which was formerly known as GeoDeepDive (e.g., Peters et al., 2017).

B.3.4. Updating proportions

Once we parse the xDD data, we calculate the relative proportions of a given parameter (here, a normalized fraction of carbonates that contain ooids) using Equation (B.2). We then compare those propor-

¹ Our size range begins at the reported value because a 2D measurement of either axis only *underestimates* true size.

² It is impossible to build a record of every ooid to ever exist. Even a random sampling, much like in polls of the electorate, likely is unattainable. Instead, the

best we can hope for is *proportionality*. See Section B.3.5 for how we calculate relative proportions.

³ Strictly speaking, we are most concerned with under-sampling the largest size fraction of ooids in any period.

⁴ Of course, such records also have spatial, temporal, and analytical biases and uncertainties (e.g., Mehra et al., 2021). Nonetheless, they are a good starting point.

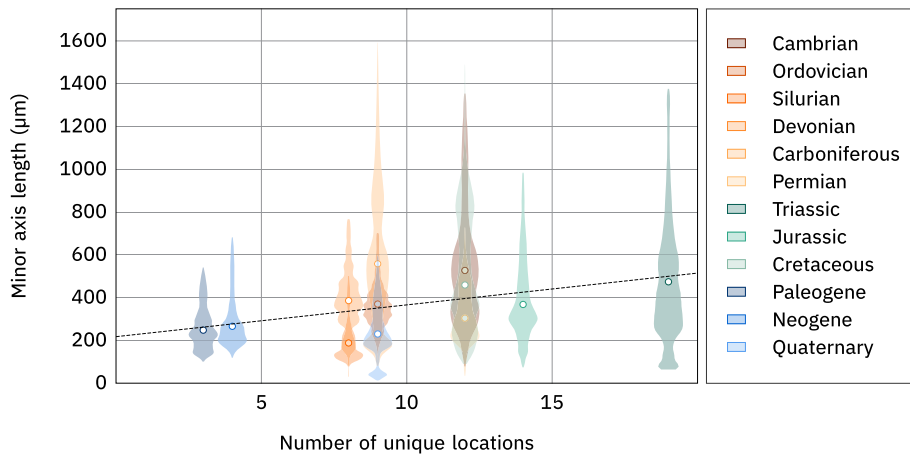


Fig. B.13. Resampled size distributions versus number of unique locations. As in Fig. B.11, the dashed line depicts a linear regression.

Table B1

Various sources (and associated parameters) to determine proportionality.

| Source | Parameter(s) | Notes about processing |
|--------------------|---|---|
| Macrostrat | Column count; volume of rock | We extract all North American sediments and metasediments using the API call presented in Husson and Peters (2018). We calculate volumes by taking the average thickness of each column and multiplying by the areal extent. |
| Ronov et al., 1980 | Volume of carbonate rock | We calculate carbonate rock volume by multiplying the volume of platforms by percent carbonate. Alternatively, one could sum up the volume of all rock and then multiply by percent carbonate. |
| xDD | Fraction of carbonates that contain ooids; normalized fraction of carbonates that contain ooids | To calculate the first parameter, we divide the sum of ooid entries by the sum of carbonate entries for each geologic period. For the normalized fraction, we multiply the first parameter by the sum of carbonate entries for that period. |

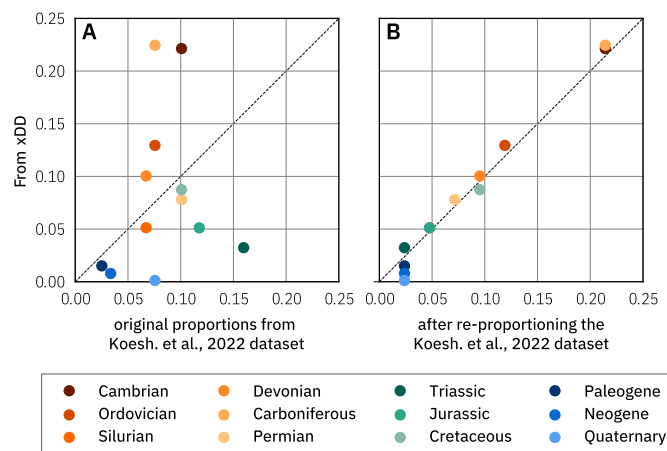


Fig. B.14. A. Per-period proportions from xDD (see Table B1) versus proportions from the Koeshidayatullah et al. (2022) ooids dataset (using number of locations, see Table B2). B. Here, the y-axis is the same as in A but the x-axis shows proportions resulting from our re-proportioning algorithm.

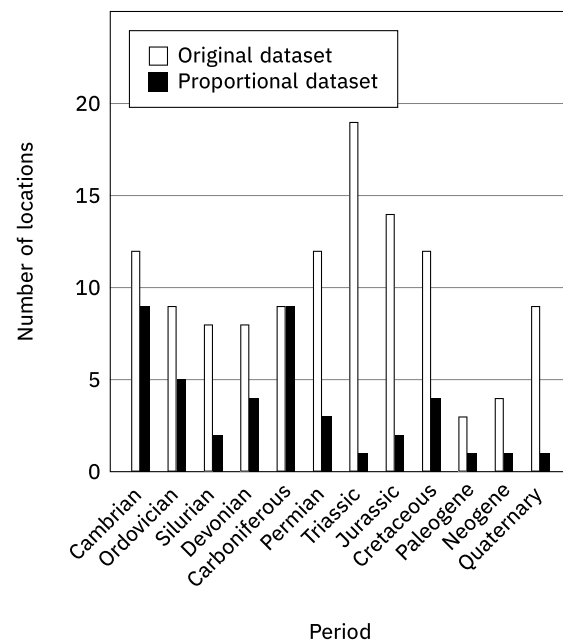


Fig. B.15. Histograms showing how the expected number of locations for a geologic period vary after re-proportioning (in grey).

2. For every ooid x from each chosen location, drawing a new minor axis length using the methodology presented in Section B.3.2.

Following this process, we create a linear regression to the data (i.e., median minor axis length versus proportion) and compile both correlation coefficients and p values, which we plot as a histogram in Fig. 9D.

tions to the relative proportions of locations per geologic period in the Koeshidayatullah et al. (2022) dataset (Fig. B.14A).

Next, we leverage a re-proportioning algorithm, which returns an array, E , where every entry, E_i , is the expected number of locations for a geologic period i (Fig. B.15). Fig. B.14B demonstrates how the proportions of the location counts in E better match the proportions from xDD.

We then run n simulations (here, $n = 1000$), each time creating a new dataset of ooids by:

1. Drawing n locations (i.e., E_i) for each period from the original ooids dataset.

Table B2

Unique locations per period in both absolute numbers and proportions. Note that proportion values are rounded to the nearest hundredth, which is why they do not sum to exactly 1.0.

| | Camb. | Ord. | Sil. | Dev. | Carb. | Perm. | Tri. | Jur. | Cret. | Paleo. | Neo. | Quat. |
|-------------|-------|------|------|------|-------|-------|------|------|-------|--------|------|-------|
| No. Locs. | 12 | 9 | 8 | 8 | 9 | 12 | 19 | 14 | 12 | 3 | 4 | 9 |
| Proportions | 0.10 | 0.08 | 0.07 | 0.07 | 0.08 | 0.10 | 0.16 | 0.12 | 0.10 | 0.03 | 0.03 | 0.08 |

B.3.5. Proportionality

For each geologic period, i , the proportion, P_i , of some parameter, z , is defined as:

$$P_i = \frac{z_i}{\sum_{k=1}^n z_k} \quad (\text{B.2})$$

where n is the number of periods being considered. Table B2 demonstrates how the number of unique locations per period are transformed into proportions using this equation.

B.4. A note on the location of giant ooids in the Early Triassic

The location of Early Triassic giant ooids in Fig. 9 differs slightly from the reconstruction from Li et al. (2021) and more closely resembles the reconstruction of Li et al. (2015) (Different authors that happen to have the same surname). There are two important differences:

1. Li et al. (2021) places the giant ooids from Germany in Panthalassa, where Li et al. (2015) places them in the Tethys. Both placements are defensible because the paleogeography of Europe is quite complicated during this time. We prefer placing the giant ooids in the Tethys because it is where the original description places the ooids (Weidlach, 2007).
2. Li et al. (2021) places a giant ooid locality in the western United States (Confusion Range, Nevada). The original manuscript on this locality (Sedlacek, 2013) describes these as large coated grains, not ooids.

Therefore, we do not include the Confusion Range in our compilation of Early Triassic giant ooid locations.

References

- Ager, D., 1973. *The Nature of the Stratigraphical Record*. Macmillan.
- Anderson, N.T., Cowan, C.A., Bergmann, K.D., 2020. A case for the growth of ancient ooids within the sediment pile. *J. Sediment. Res.* 90, 843–854.
- Batchelor, M.T., Burne, R.V., Henry, B.I., Li, F., Paul, J., 2018. A biofilm and organomineralisation model for the growth and limiting size of ooids. *Sci. Rep.* 8, 559.
- Beaupré, S.R., Roberts, M.L., Burton, J.R., Summons, R.E., 2015. Rapid, high-resolution ^{14}C chronology of ooids. *Geochim. Cosmochim. Acta* 159, 126–138.
- Berner, R.A., 2004. A model for calcium, magnesium and sulfate in seawater over Phanerozoic time. *Am. J. Sci.* 304, 438–453.
- Bialik, O.M., Sisma-Ventura, G., Vogt-Vincent, N., Silverman, J., Katz, T., 2022. Role of oceanic abiotic carbonate precipitation in future atmospheric CO₂ regulation. *Sci. Rep.* 12, 15970.
- Blakey, R.C., Ranney, W.D., 2017. *Ancient Landscapes of Western North America: A Geologic History with Paleogeographic Maps*. Springer.
- Blakey, R.C., Fielding, C., Frank, T., Isbell, J., et al., 2008. Gondwana paleogeography from assembly to breakup—a 500 my odyssey. *Geol. Soc. Am. Spec. Pap.* 441, 1–28.
- Broecker, W.S., Takahashi, T., 1966. Calcium carbonate precipitation on the Bahama Banks. *J. Geophys. Res.* 71, 1575–1602.
- Burton, E.A., Walter, L.M., 1987. Relative precipitation rates of aragonite and mg calcite from seawater: temperature or carbonate ion control? *Geology* 15, 111–114.
- Coggon, R.M., Teagle, D.A., Smith-Duque, C.E., Alt, J.C., Cooper, M.J., 2010. Reconstructing past seawater Mg/Ca and Sr/Ca from mid-ocean ridge flank calcium carbonate veins. *Science* 327, 1114–1117.
- Comas-Bru, L., Rehfeld, K., Roesch, C., Amirnezhad-Mozhdehi, S., Harrison, S.P., At-sawaranunt, K., Ahmad, S.M., Brahim, Y.A., Baker, A., Bosomworth, M., et al., 2020. SISALv2: a comprehensive speleothem isotope database with multiple age-depth models. *Earth Syst. Sci. Data* 12, 2579–2606.
- Davies, P., Kinsey, D., 1977. Holocene reef growth—One Tree Island, Great Barrier Reef. *Mar. Geol.* 24, M1–M11.
- Davies, P.J., Bubela, B., Ferguson, J., 1978. The formation of ooids. *Sedimentology* 25, 703–730.
- Dickson, J., 2002. Fossil echinoderms as monitor of the Mg/Ca ratio of Phanerozoic oceans. *Science* 298, 1222–1224.
- Dunlea, A.G., Murray, R.W., Santiago Ramos, D.P., Higgins, J.A., 2017. Cenozoic global cooling and increased seawater mg/ca via reduced reverse weathering. *Nat. Commun.* 8, 844.
- Eardly, A., 1938. *Sediments of Great Salt Lake*. AAPG, Utah.
- El-Sammak, A., Tucker, M., 2002. Ooids from Turkey and Egypt in the Eastern Mediterranean and a love-story of Antony and Cleopatra. *Facies* 46, 217–227.
- Ferguson, J., Bubela, B., Davies, P.J., 1978. Synthesis and possible mechanism of formation of radial carbonate ooids. *Chem. Geol.* 22, 285–308.
- Gallagher, S., Reuning, L., Himmler, T., Henderiks, J., De Vleeschouwer, D., Groeneveld, J., Lari, A.R., Fulthorpe, C., Bogus, K., Renema, W., et al., 2018. The enigma of rare Quaternary oolites in the Indian and Pacific Oceans: a result of global oceanographic physicochemical conditions or a sampling bias? *Quat. Sci. Rev.* 200, 114–122.
- Geyman, E.C., Maloof, A.C., 2019. A diurnal carbon engine explains ^{13}C -enriched carbonates without increasing the global production of oxygen. *Proc. Natl. Acad. Sci.* 116, 24433–24439.
- Geyman, E.C., Maloof, A.C., 2021. Facies control on carbonate $\delta^{13}\text{C}$ on the Great Bahama Bank. *Geology* 49, 1049–1054.
- Geyman, E.C., Wu, Z., Nadeau, M.D., Edmondson, S., Turner, A., Purkis, S.J., Howes, B., Dyer, B., Ahm, A.S.C., Yao, N., et al., 2022. The origin of carbonate mud and implications for global climate. *Proc. Natl. Acad. Sci.* 119, e2210617119.
- Gothmann, A.M., Stolarski, J., Adkins, J.F., Schoene, B., Dennis, K.J., Schrag, D.P., Mazur, M., Bender, M.L., 2015. Fossil corals as an archive of secular variations in seawater chemistry since the Mesozoic. *Geochim. Cosmochim. Acta* 160, 188–208.
- Heller, P.L., Komar, P.D., Pevear, D.R., 1980. Transport processes in ooid genesis. *J. Sediment. Res.* 50, 943–951.
- Higgins, J.A., Blättler, C.L., Lundstrom, E., Santiago-Ramos, D., Akhtar, A., Ahm, A.C., Bialik, O., Holmden, C., Bradbury, H., Murray, S., et al., 2018. Mineralogy, early marine diagenesis, and the chemistry of shallow-water carbonate sediments. *Geochim. Cosmochim. Acta* 220, 512–534.
- Howes, B., Mehra, A., Maloof, A.C., 2021. Three-dimensional morphometry of ooids in oolites: a new tool for more accurate and precise paleoenvironmental interpretation. *J. Geophys. Res., Earth Surf.* 126, e2020JF005601.
- Husson, J., Peters, S., 2018. Nature of the sedimentary rock record and its implications for Earth system evolution. *Emerg. Top. Life Sci.* 2, 125–136.
- Jamison-Todd, S., Stein, N., Overeem, I., Khalid, A., Trower, E.J., 2020. Hurricane deposits on carbonate platforms: a case study of hurricane irma deposits on Little Ambergris Cay, Turks and Caicos Islands. *J. Geophys. Res., Earth Surf.* 125, e2020JF005597.
- Kageyama, M., Braconnot, P., Bopp, L., Caubel, A., Foujols, M.A., Guilyardi, E., Khodri, M., Lloyd, J., Lombard, F., Mariotti, V., et al., 2013. Mid-Holocene and Last Glacial Maximum climate simulations with the IPSL model—part I: comparing IPSL_CM5A to IPSL_CM4. *Clim. Dyn.* 40, 2447–2468.
- Keller, C.B., Husson, J.M., Mitchell, R.N., Bottke, W.F., Gernon, T.M., Boehnke, P., Bell, E.A., Swanson-Hysell, N.L., Peters, S.E., 2019. Neoproterozoic glacial origin of the Great Unconformity. *Proc. Natl. Acad. Sci.* 116, 1136–1145.
- Key, R.M., Kozyr, A., Sabine, C.L., Lee, K., Wanninkhof, R., Bullister, J.L., Feely, R.A., Millero, F.J., Mordy, C., Peng, T.H., 2004. A global ocean carbon climatology: results from Global Data Analysis Project (GLODAP). *Glob. Biogeochem. Cycles* 18.
- Kiessling, W., Flügel, E., Golonka, J., 2003. Patterns of Phanerozoic carbonate platform sedimentation. *Lethaia* 36, 195–225.
- Koeshidayatullah, A., Trower, E.J., Li, X., Mukerji, T., Lehrmann, D.J., Morsilli, M., Al-Ramadan, K., Payne, J.L., 2022. Quantitative evaluation of the roles of ocean chemistry and climate on ooid size across the Phanerozoic: Global versus local controls. *Sedimentology* 69, 2486–2506.
- Kruse, F., 1996. Identification and mapping of minerals in drill core using hyperspectral image analysis of infrared reflectance spectra. *Int. J. Remote Sens.* 17, 1623–1632.
- Laughrey, C.D., Harper, J.A., 2012. Upper Cambrian Gatesburg formation of central and western Pennsylvania. In: AAPG Special Volumes.
- Lehrmann, D.J., Minzioni, M., Li, X., Yu, M., Payne, J.L., Kelley, B.M., Schaaf, E.K., Enos, P., 2012. Lower Triassic oolites of the Nanpanjiang Basin, south China: facies architecture, giant ooids, and diagenesis—implications for hydrocarbon reservoirs. *AAPG Bull.* 96, 1389–1414.
- Li, F., Yan, J., Chen, Z.Q., Ogg, J.G., Tian, L., Korngreen, D., Liu, K., Ma, Z., Woods, A.D., 2015. Global oolite deposits across the Permian-Triassic boundary: a synthesis and implications for palaeoceanography immediately after the end-Permian biocrisis. *Earth-Sci. Rev.* 149, 163–180.

- Li, X., Trower, E.J., Lehrmann, D.J., Minzoni, M., Kelley, B.M., Schaal, E.K., Altiner, D., Yu, M., Payne, J.L., 2021. Implications of giant ooids for the carbonate chemistry of Early Triassic seawater. *Geology* 49, 156–161.
- Loreau, J.P., Purser, B., 1973. Distribution and ultrastructure of Holocene ooids in the Persian Gulf. In: *The Persian Gulf: Holocene Carbonate Sedimentation and Diagenesis in a Shallow Epicontinental Sea*. Springer, pp. 279–328.
- Lorenzen, W.E., Cline, H.E., 1987. Marching cubes: a high resolution 3D surface construction algorithm. *Comput. Graph.* 21, 163–169.
- MacLennan, S., Park, Y., Swanson-Hysell, N., Maloof, A., Schoene, B., Gebreslassie, M., Antilla, E., Tesema, T., Alene, M., Haileab, B., 2018. The arc of the Snowball: U-Pb dates constrain the Islay anomaly and the initiation of the Sturtian glaciation. *Geology* 46, 539–542.
- Mandelbrot, B., 1967. How long is the coast of Britain? Statistical self-similarity and fractional dimension. *Science* 156, 636–638.
- Manzuk, R.A., Singh, D., Mehra, A., Geyman, E.C., Edmonson, S., Maloof, A.C., 2022. A high-resolution multispectral macro-imager for geology and paleontology. *GSA Today* 32, 4–9.
- Martin, R.E., 1995. Cyclic and secular variation in microfossil biomineralization: clues to the biogeochemical evolution of Phanerozoic oceans. *Glob. Planet. Change* 11, 1–23.
- McKirdy, D.M., Burgess, J.M., Lemon, N.M., Yu, X., Cooper, A.M., Gostin, V.A., Jenkins, R.J., Both, R.A., 2001. A chemostratigraphic overview of the late Cryogenian interglacial sequence in the Adelaide Fold-Thrust Belt, South Australia. *Precambrian Res.* 106, 149–186.
- Meakin, P., Jamtveit, B., 2010. Geological pattern formation by growth and dissolution in aqueous systems. *Proc. R. Soc. A, Math. Phys. Eng. Sci.* 466, 659–694.
- Mehra, A., Keller, C., Zhang, T., Tosca, N., MacLennan, S., Sperling, E., Farrell, U., Brocks, J., Canfield, D., Cole, D., et al., 2021. Curation and analysis of global sedimentary geochemical data to inform Earth history. *GSA Today*.
- Mehra, A., Howes, B., Manzuk, R., Spatzier, A., Samuels, B.M., Maloof, A.C., 2022. A novel technique for producing three-dimensional data using serial sectioning and semi-automatic image classification. *Microsc. Microanal.* 28, 2020–2035.
- Milliman, J.D., 1969. Carbonate sedimentation on four southwestern Caribbean atolls and its relation to the “oolite problem”. *Gulf Coast Assoc. Geol. Soc. Trans.* 19, 195–206.
- Mono, P., Hoffmann, R., Wissak, M., Lokier, S.W., Pederson, C.L., Hennhofer, D., Diaz, M.R., Swart, P., Nehrke, G., Immenhauser, A., 2023. Microborings reveal alternating agitation, resting and sleeping stages of modern marine ooids. *Sedimentology*.
- O’Connell, B., Wallace, M.W., Hood, A.V., Rebbechi, L., Brooks, H.L., 2022. Deep water cuspatate stromatolites of the Cryogenian Trezona Formation. *Geobiology* 20, 194–215.
- Odyke, B.N., Walker, J.C., 1992. Return of the coral reef hypothesis: basin to shelf partitioning of CaCO_3 and its effect on atmospheric CO_2 . *Geology* 20, 733–736.
- Odyke, B.N., Wilkinson, B.H., 1988. Surface area control of shallow cratonic to deep marine carbonate accumulation. *Paleoceanography* 3, 685–703.
- Odyke, B.N., Wilkinson, B.H., 1990. Paleolatitude distribution of Phanerozoic marine ooids and cements. *Palaeogeogr. Palaeoclimatol. Palaeoecol.* 78, 135–148.
- Park, Y., Swanson-Hysell, N.L., MacLennan, S.A., Maloof, A.C., Gebreslassie, M., Tremblay, M.M., Schoene, B., Alene, M., Antilla, E.S., Tesema, T., et al., 2020. The lead-up to the Sturtian Snowball Earth: Neoproterozoic chemostratigraphy time-calibrated by the Tambien Group of Ethiopia. *GSA Bull.* 132, 1119–1149.
- Payne, J.L., Lehrmann, D.J., Christensen, S., Wei, J., Knoll, A.H., 2006a. Environmental and biological controls on the initiation and growth of a Middle Triassic (Anisian) reef complex on the Great Bank of Guizhou, Guizhou Province, China. *Palaios* 21, 325–343.
- Payne, J.L., Lehrmann, D.J., Wei, J., Knoll, A.H., 2006b. The pattern and timing of biotic recovery from the end-Permian extinction on the Great Bank of Guizhou, Guizhou Province, China. *Palaios* 21, 63–85.
- Peters, S.E., Gaines, R.R., 2012. Formation of the ‘Great Unconformity’ as a trigger for the Cambrian explosion. *Nature* 484, 363–366.
- Peters, S.E., Husson, J.M., Wilcots, J., 2017. The rise and fall of stromatolites in shallow marine environments. *Geology* 45, 487–490.
- Peters, S.E., Husson, J.M., Czaplewski, J., 2018. Macrostrat: a platform for geological data integration and deep-time Earth crust research. *Geochem. Geophys. Geosyst.* 19, 1393–1409.
- Pruss, S.B., Finnegan, S., Fischer, W.W., Knoll, A.H., 2010. Carbonates in skeleton-poor seas: new insights from Cambrian and Ordovician strata of Laurentia. *Palaios* 25, 73–84.
- Rao, M.S., 1964. Some aspects of continental shelf sediments off the East coast of India. *Mar. Geol.* 1, 59–87.
- Rausch, S., Böhm, F., Bach, W., Klügel, A., Eisenhauer, A., 2013. Calcium carbonate veins in ocean crust record a threefold increase of seawater Mg/Ca in the past 30 million years. *Earth Planet. Sci. Lett.* 362, 215–224.
- Ridgwell, A., 2005. A Mid Mesozoic Revolution in the regulation of ocean chemistry. *Mar. Geol.* 217, 339–357.
- Ries, J.B., 2010. Geological and experimental evidence for secular variation in seawater Mg/Ca (calcite-aragonite seas) and its effects on marine biological calcification. *Biogeosciences* 7, 2795–2849.
- Ronov, A., Khain, V., Balukhovsky, A., Seslavinsky, K., 1980. Quantitative analysis of Phanerozoic sedimentation. *Sediment. Geol.* 25, 311–325.
- Rose, C.V., Maloof, A.C., Schoene, B., Ewing, R.C., Linnemann, U., Hofmann, M., Cottle, J.M., 2013. The end-cryogenian glaciation of south Australia. *Geosci. Can.* 40, 256–293.
- Rowland, S.M., Shapiro, R.S., 2002. Reef patterns and environmental influences in the Cambrian and earliest Ordovician. *SEPM 72*.
- Sadler, P.M., 1981. Sediment accumulation rates and the completeness of stratigraphic sections. *J. Geol.* 89, 569–584.
- Sandberg, P.A., 1975. New interpretations of Great Salt Lake ooids and of ancient non-skeletal carbonate mineralogy. *Sedimentology* 22, 497–537.
- Sandberg, P.A., 1983. An oscillating trend in Phanerozoic non-skeletal carbonate mineralogy. *Nature* 305, 19–22.
- Schumer, R., Jerolmack, D.J., 2009. Real and apparent changes in sediment deposition rates through time. *J. Geophys. Res., Earth Surf.* 114.
- Sedlacek, A., 2013. Strontium isotope stratigraphy and carbonate sedimentology of the latest Permian to Early Triassic in the Western United States, northern Iran, and southern China. Ph.D Dissertation, Graduate School of the Ohio State University.
- Simpson, C., 2021. Adaptation to a viscous snowball Earth ocean as a path to complex multicellularity. *Am. Nat.* 198, 590–609.
- Singh, U., 1987. Ooids and cements from the late Precambrian of the Flinders Ranges, South Australia. *J. Sediment. Res.* 57, 117–127.
- Sipos, A.A., Domokos, G., Jerolmack, D.J., 2018. Shape evolution of ooids: a geometric model. *Sci. Rep.* 8, 1–7.
- Smith, S., Pesret, F., 1974. Processes of Carbon Dioxide Flux in the Fanning Island Lagoon.
- Trower, E.J., 2020. The enigma of Neoproterozoic giant ooids—fingerprints of extreme climate? *Geophys. Res. Lett.*, e2019GL086146.
- Trower, E.J., Lamb, M.P., Fischer, W.W., 2017. Experimental evidence that ooid size reflects a dynamic equilibrium between rapid precipitation and abrasion rates. *Earth Planet. Sci. Lett.* 468, 112–118.
- Trower, E.J., Cantine, M.D., Gomes, M.L., Grotzinger, J.P., Knoll, A.H., Lamb, M.P., Lingappa, U., O'Reilly, S.S., Present, T.M., Stein, N., et al., 2018. Active ooid growth driven by sediment transport in a high-energy shoal, Little Ambergris Cay, Turks and Caicos Islands. *J. Sediment. Res.* 88, 1132–1151.
- Trower, E.J., Lamb, M.P., Fischer, W.W., 2019. The origin of carbonate mud. *Geophys. Res. Lett.* 46, 2696–2703.
- Trower, E.J., Bridgers, S.L., Lamb, M.P., Fischer, W.W., 2020. Ooid cortical stratigraphy reveals common histories of individual co-occurring sedimentary grains. *J. Geophys. Res., Earth Surf.* 125, e2019JF005452.
- vS Hood, A., Planavsky, N.J., Wallace, M.W., Wang, X., 2018. The effects of diagenesis on geochemical paleoredox proxies in sedimentary carbonates. *Geochim. Cosmochim. Acta* 232, 265–287.
- Weidlich, O., 2007. PTB mass extinction and earliest Triassic recovery overlooked? New evidence for a marine origin of Lower Triassic mixed carbonate–siliciclastic sediments (Rogenstein Member), Germany. *Palaeogeogr. Palaeoclimatol. Palaeoecol.* 252, 259–269.
- Wilkinson, B.H., 2015. Precipitation as meteoric sediment and scaling laws of bedrock incision: assessing the Sadler effect. *J. Geol.* 123, 95–112.
- Wilkinson, B.H., Given, R.K., 1986. Secular variation in abiotic marine carbonates: constraints on Phanerozoic atmospheric carbon dioxide contents and oceanic Mg/Ca ratios. *J. Geol.* 94, 321–333.
- Yao, L., Aretz, M., Wignall, P.B., Chen, J., Vachard, D., Qi, Y., Shen, S., Wang, X., 2020. The longest delay: re-emergence of coral reef ecosystems after the Late Devonian extinctions. *Earth-Sci. Rev.* 203, 103060.
- Zeebe, R.E., 2012. History of seawater carbonate chemistry, atmospheric CO₂, and ocean acidification. *Annu. Rev. Earth Planet. Sci.* 40, 141–165.
- Zeebe, R.E., Tyrrell, T., 2019. History of carbonate ion concentration over the last 100 million years II: revised calculations and new data. *Geochim. Cosmochim. Acta* 257, 373–392.
- Zhang, C., Govindaraju, V., Borchardt, J., Foltz, T., Ré, C., Peters, S., 2013. GeoDeepDive: statistical inference using familiar data-processing languages. In: *Proceedings of the 2013 ACM SIGMOD International Conference on Management of Data*, pp. 993–996.
- Zhong, S., Mucci, A., 1989. Calcite and aragonite precipitation from seawater solutions of various salinities: precipitation rates and overgrowth compositions. *Chem. Geol.* 78, 283–299.